Theoretical and experimental investigations on the Child-Langmuir-limited current

Studi teorici e sperimentali sulla corrente limite di Child-Langmuir

Relatore:
Prof. Ing. **Piergiorgio Sonato**, Università di Padova

Correlatori:
Dott. **Gianluigi Serianni**, Consorzio RFX
Dott. **Pierluigi Veltri**, Consorzio RFX

Laureando:
Fabio Spinazzè, Matricola 1106549

A.A. 2016-2017

Abstract

ITER, the international fusion reactor project, entered the construction phase in 2013, next to Cadarache in south France. The university of Padua, partner of the consorzio RFX, participates in the construction of one of the main parts: the neutral beam injector. This work regards the NIO1 experiment, a prototype of the plasma source of the injector and an ideal test bench for the project. In this thesis an analytical and adimensional model of the accelerating beam is presented. It agrees with experimental datas, shows precisely the maximum obtainable performances but foremost, with this model, it is possible to generalize those results for any given particle, at any energy level and scale.

The first section of this thesis introduces the physics behind the nuclear fusion and the technologies required in the process. Then the Richardson's and Child's laws are recalled since they provide the basins to understand the hypothesis and the developments of the theory presented in the second section and the results showed in the third. In the second section, the monodimensional model of a charged particle beam which accelerates under the influence of the electric field between two grids is presented. Thanks to the analytical solution of the model's equations it is possible to describe the steady state beam behavior as a function of time or space. This applies to particles with any mass and any initial speed. Furthermore, the model is generalized to a two particle case, as it is between the first two grids of the typical negative ion accelerator.

The last section compares the experimental results with the model and proposes an explanation of the saturation phenomenon seen at maximum extraction voltage through a thermionic emission analogy.

Sommario

ITER, il progetto internazionale di reattore a fusione nucleare è in costruzione dal 2013 nel sud della Francia. L'università di Padova, una dei soci del consorzio RFX partecipa alla costruzione di una sua parte fondamentale: l'iniettore di fasci neutri. Questo lavoro si pone nell'ambito dell'esperimento NIO1, un prototipo della sorgente dell'iniettore, banco prova ideale per migliorare il progetto. In particolare, è presentato un modello analitico e adimensionale del fascio durante le fasi di accelerazione, capace non solo di confermare i dati sperimentali e di conoscere con precisione le massime prestazioni ottenibili ma anche di generalizzare tali risultati per particelle qualsiasi ed esperimenti ad energie e scale arbitrarie.

Questa tesi si apre con un capitolo introduttivo in cui, oltre ad una breve panoramica sulla fisica della fusione e degli apparati richiesti, sono richiamate le leggi di Richardson e di Child. Queste ultime sono un punto di partenza necessario per comprendere le premesse e gli sviluppi della teoria presentata nel secondo capitolo e i risultati contenuti nel terzo.

Nel secondo capitolo è presentato il modello monodimensionale di un fascio di particelle ionizzate che viene accelerato dal campo elettrico presente tra due griglie. Attraverso la soluzione analitica delle equazioni che compongono il modello è possibile descrivere il comportamento del fascio in regime stazionario in funzione del tempo o della posizione, per particelle di massa qualsiasi e per velocità di ingresso positive o nulle. Successivamente, il modello viene esteso al caso in cui sono presenti due portatori di carica come avviene tra le prime due griglie di un tipico acceleratore di ioni negativi.

L'ultimo capitolo confronta i risultati sperimentali con gli andamenti teorici predetti dal modello e propone una spiegazione al fenomeno di saturazione osservato alle massime tensioni di estrazione attraverso un'analogia con l'emissione termoionica.

Contents

1 Introduction

1.1 Power from fusion

Regular stars are natural fusion reactors, fueled by the most common chemical elements of the universe. They sustain the same reactions for billions of years, slowly converting some of their mass into energy and light. These reactions were discovered almost a century ago and since then, nations, scientists, engineers, and more recently businessmen started to dream to steal this prometheus fire.

History teaches us that energy availability is one of the strongest factors that influences social and scientific advancement. Currently, our energy needs are growing and highly expensive, nevertheless some nations, Italy for instance, depend on others' resources.

Nuclear fission energy has secured the most advanced nations' growth during the last half century. AIEA estimates that the worldwide nominal power will increase from the existing 374 GW to at least 453 GW by 2020. In Europe though, this trend will be probably weaker, due to political reasons, Germany and Switzerland have planned the decommissioning of their power plants, like Spain and Belgium did with some old sites.

In the meantime, energy from renewables sources kept climbing the EU electricity mix, and now it is beyond 30%. A doubling of its share is unlikely, because of grid stability issues, but it is not impossible [1]. In 2014 for example, 43.1% of italian electricity demand was covered by renewables, and only 4.6% by nuclear fission [2] [3]. Under a more economic perspective, intermittent and unpredictables power sources currently rely on strong grids, and baseline production is made cheap by big fossil fuels power plants. A solution that helps replacing these sources with a low-carbon electric power production, can be represented by the nuclear fusion.
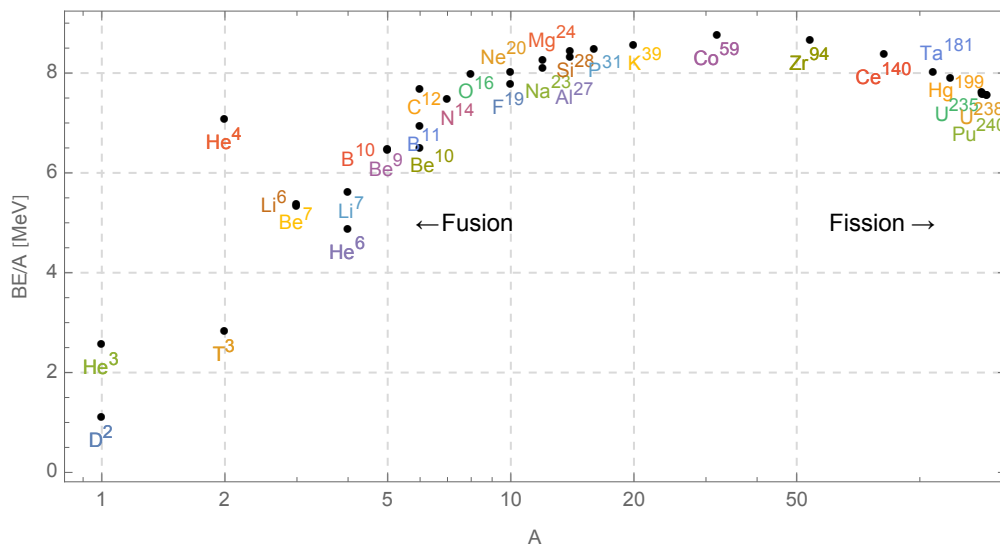
Figure 1: Binding Energy of nuclei vs Atomic number, abscissae in log scale.
Higher energy gap means more energy-per-nucleons involved in the nuclear reaction.

As with fission, nuclear fusion produces energy by freeing the binding energy of atomic nuclei. In this case though, two light nuclei can be bound together to create a heavier nucleus. Because of their positive charge, the Coulomb repulsion between nuclei is very strong and particles need to reach high energy to get close enough for the fusion. At quantum scales, Strong Interaction

overcomes the electrostatic force, and the Tunnel Effect allows the fusion of the nuclei even if the average kinetic energy is lower than the potential barrier. Several exothermic fusion reactions are known: the present fusion research is focused on the deuterium-tritium (D-T) reaction due to the higher cross section compared to other reactions. The total energy is divided between helium and neutron kinetic energy, as reported in the following equation:

$$^2_1D \; + \; ^3_1T \rightarrow \; ^4_2He \; (3.5 \text{ MeV}) + n \; (14.1 \text{ MeV})$$
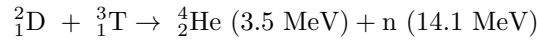
While tritium is available in water, lithium is an unstable isotope with a short lifetime (about 12 years). However, tritium can be produced from lithium, which is widespread on the earth crust. This element easily reacts with the incoming neutrons as follows:

$$^6_3Li \; + n \rightarrow \; ^3_1T \; + \; ^4_2He \; + 4.78 \text{ MeV}$$

$$^7_3Li \; + n \rightarrow \; ^3_1T \; + \; ^4_2He \; + n - 2.47 \text{ MeV}$$
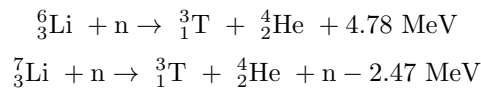
There are currently many lines of research regarding the plasma confinement technology and the nuclear reactants, some supported by private industries and investors and others financed by government and international partnerships. Among them, the Tokamak configuration was developed in USSR in 1950's and due to the remarkable performances reached, it is considered the most promising configuration to achieve nuclear fusion for energy purposes.

Tokamaks are toroidal machines in which plasmas are confined by a strong toroidal magnetic field and a lower poloidal field to avoid drifts that can lead to a separation of species and loss of plasma. The former is produced by several toroidal coils, while the latter is induced by an axial coil. In a toroidal configuration, produced Helium nuclei are supposed to cede energy to deuterium or tritium nuclei through collisions, while neutrons, that can not be magnetically confined due to their neutral charge, will cede their energy to the blanket. In this way, kinetic energy is transformed into thermal energy which will be further converted in electricity and sold in future commercial fusion power plants.

1.2 Plasma heating and ignition

Every power plant needs some auxiliary power in order to stay operational. Usually this power accounts for few percents of the net produced power. For a thermoelectric plant, this power is needed for pumps, compressors, and control drives while, for a fusion reactor like ITER, auxiliary power takes much more of the share. Although the toroidal and poloidal fields are created by currents in superconducting inductors, a considerable amount of power is spent to keep the Nb_3Sn coils at 5 K (very near to a hotter-than-stars plasma) and additional losses can be localized in the power supply. [4]

However, the true power consumption of any fusion reactor (50 MW for ITER) is due to the plasma heating system. In order to reach and maintain the fusion temperature inside the Tokamak, reactors around the world use several techniques, some of which are:

- **Ohmic heating**. Electrical currents are induced via transformer action in the plasma and produce Joule losses. This method has two limitations: it is pulsed and its effectiveness decreases as the plasma heats up because plasma resistivity depends on temperature as $T^{-3/2}$. For this reason it is used only during the pre-heating phase and power up to few MW.

- **Radio-Frequency heating**. As the plasma particles rotate around magnetic field lines in the chamber, electromagnetic waves can selectively damp or resonate with the motion, changing the kinetic energy of some particles. Switching losses in the power source limit the RF power that can be sent to the plasma to few tens of MW. ITER uses three RF systems at different frequencies: the 30-100 MHz module heats ions while the others are focused on electrons at frequency bands of 1-8 GHz and 100-200 GHz.

- **Neutral beam heating**. To penetrate the strong magnetic field in the chamber, a beam of fast moving neutral atoms is aimed at the plasma where it loses electrons, merges with the confined ions and transfers kinetic energy to them. The only way to create such beam is to produce a large amount of ions first, then accelerate them in an electric field up to the desired speed and finally neutralize them with electrons.

  Consorzio RFX was called to develop the prototype of injectors that will be used in ITER: for this purpose, PRIMA (Padova Research ITER Megavolt Accelerator) facility has been established. It will host two experiments: SPIDER (Source for the Production of Ion of deuterium Extracted from an RF plasma), which is the prototype of the ion source that will be used for the complete injector, and MITICA (Megavolt ITER Injector and Concept Advance) which is the actual complete injector. [5]

  ITER shall require 16.5 MW of power, so a 40 A deuterium ions current needs to be extracted. To achieve this extracted current, it is expected to obtain a current density of 280 A/m^2, accelerated up to an energy of 1 MeV.
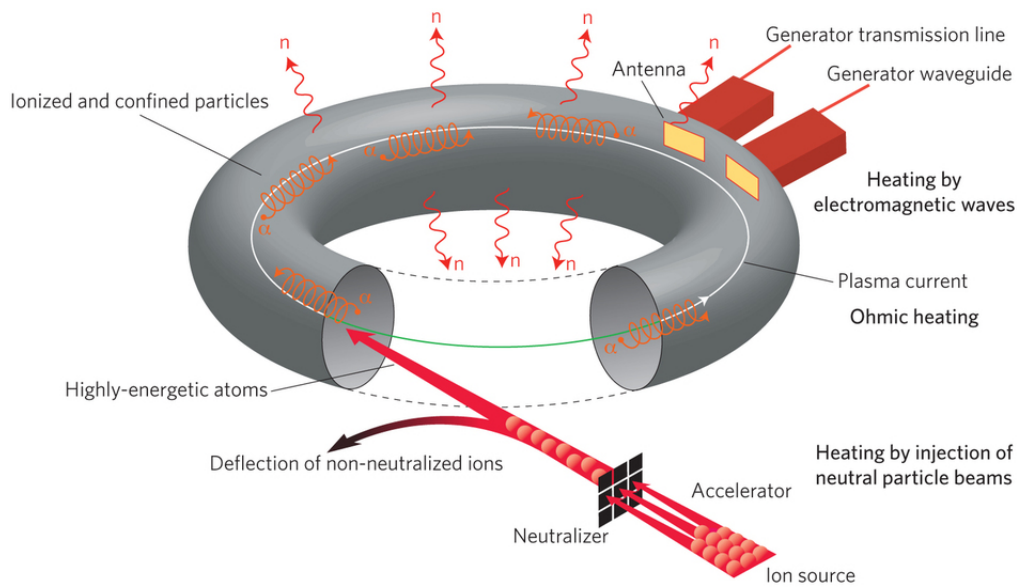

Figure 2: Different sources of heating in a Tokamak. Image courtesy of [6]

In conclusion, a useful parameter to evaluate the ratio between gross power produced by the fusion and power needed to the heat the plasma is called energy gain factor:

$$Q = \frac{P_{\text{fusion}}}{P_{\text{heat}}} \simeq \frac{1}{\eta \ f_{\text{re}}}$$

The condition in which $Q = 1$, named **break-even**, happens when the energy produced in fusion reaction exactly matches the external heating power. Considering typical efficiency η of the double energy transformation and the fraction f_{re} of the total power that is recirculating through the heating system, Q should be between 15 and 30 for practical reactors.

Ignition of plasma is reached when all the thermal energy needed to sustain the reaction comes from the fusion itself, so $P_{\text{heat}} \to 0$, $Q \to \infty$. The ignition is the most convenient regime for a thermonuclear reactor, however it is not strictly needed as an external heating system helps keeping plasma stability. Currently, the only known man-made item that achieved $Q > 1$ is the Ivy Mike hydrogen bomb.

1.3   Ion production

Currently, there are several ion sources available to scientists: every one has its own pros and cons which defines the most suitable application, e.g. plasma sources excite matter to its fourth

state in order to create ions. Among them, **inductively coupled plasma** (ICP) and hot cathode sources are the most used in ion accelerators around the world. The former excites molecules with fast changing (GHz range) electromagnetic field thus it creates a hot spot at the coil center where fast electrons are produced. The latter makes use of a hot cathode that emits slow electrons by thermionic effect. This technology is simpler, but the cathode must withstand temperature as high as 1800-2400 K in order to reach the desired current and is coated with rare and expensive materials like thorium or lanthanum. Lastly, while the ICP source is physically separated from the plasma it produces, the hot cathode must be inside the chamber exposed to ion bombardment and oxidation. Also, it can release impurity and eventually, it has to be replaced.

The remarkable requirements for the ITER Neutral Beam forced designers not only to focus on negative Ion because of their larger cross section during the neutralization process, but also to choose an ICP source instead of thermionic emission because the best reliability and the longest lifespan are needed. [7]

ICP, in particular, offers two kinds of ion production:

- **Volume production** takes place inside the plasma and it can be divided into two steps: first H_2 molecules are vibrationally excited by collisions with fast electrons ($E > 20$ eV), then negative ions are produced by dissociative attachment between those excited molecules and cold electrons ($E < 2$ eV). [8]

$$H_2 + e_{\text{fast}} \rightarrow H_2^* + e, \qquad H_2^* + e_{\text{slow}} \rightarrow H^- + H^0$$

  Although, there are several processes that lead to the neutralization of such ions, in particular detachment is dominant at electron energy above 1 eV. To reduce H^- losses, the plasma chamber is divided in two volumes by a vertical magnetic field: the hotter region witch is under the influence of the RF heating system that produces fast electrons and excites molecules, and the **extraction zone** witch is unreachable by fast electrons, and where negative ions are produced.
  Numerical studies by Vetri et al. [9] confirmed that in NIO1 only H^- produced in the extraction region, eventually reach the grid and they are extracted as such. The others that are produced in the far left region are soon and easily neutralized by fast electrons. The overall ionization degree in the two regions is under 1% with its maximum at the center of the RF coils. This means that only 1 particle out of 100 is ionized (positively or negatively) and for this reason the plasma is said cold.

- **Surface production**. It has been demonstrated [8] that caesium vapor deposition in the source chamber causes a 3-10 times enhancement of negative ion production. Caesium produces a thin layer over the walls, thus causing a lowering of the work function. Ion production has to be improved especially close to the grids, where the H^-, produced by the collisions of H^0 with the source walls and plasma grid, can be promptly extracted. It has been calculated that with such deposition in the NIO1 chamber, H^0 atoms near the PG have a 30% chance of becoming H^- thus increasing dramatically the maximum ion current.

Negative ions sources usually prevent charged particles from hitting the walls by a technique called *magnetic bottle*: permanent magnets placed behind the walls of the source bend magnetic field lines to form an array of cusps and domes that force charged particles towards the center of the camber.
Another common feature is that the electric potential of the source body must be kept negative with respect to the grounded forward sections of the accelerator. By doing so, the highest voltage is located in a relatively small and closed section of the experiment, increasing safety and reducing electrostatic losses at the same time.

Consequently, ICP plasma chambers are basically like the one in figure 3. In particular, designers of NIO1 came up with the design shown in figure 4 and 5.
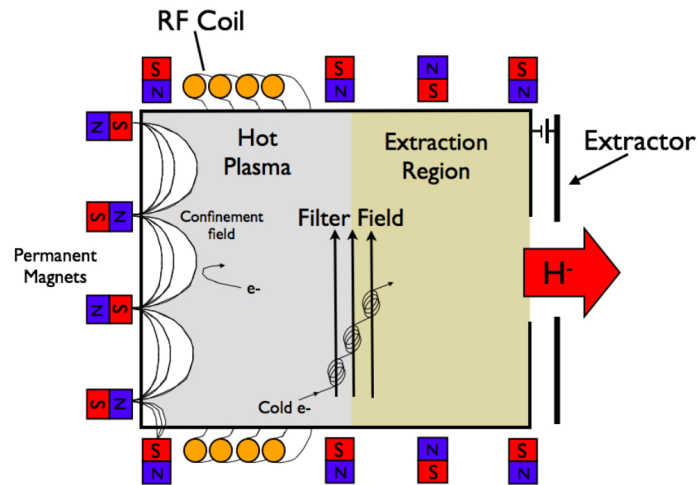
Figure 3: Conceptual representation of a negative ion source. The presence of two zones separated by the filter field can be noticed.
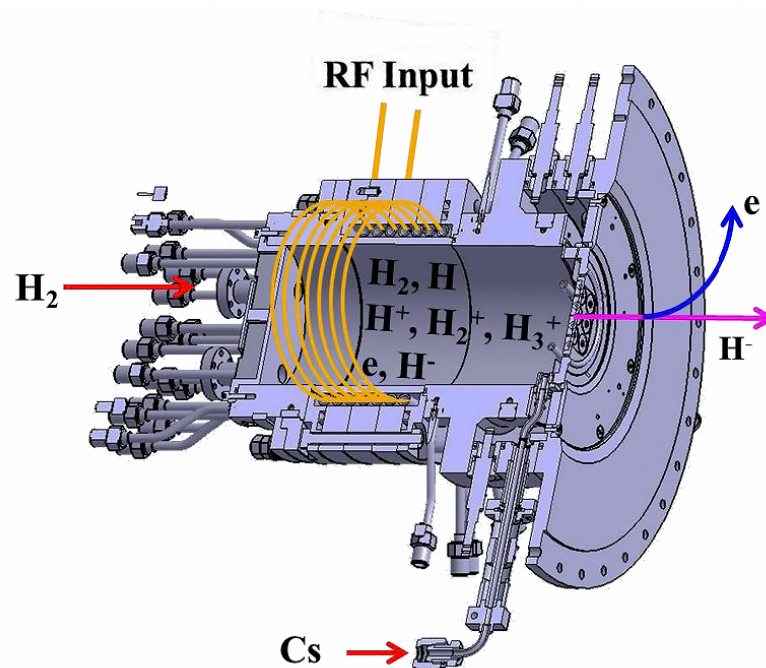

Figure 4: Cutaway of the NIO1 source. It features the same concept of the ITER source at smaller scale, allowing designers to improve the project faster.

1.4 Acceleration

Negative ions produced by the source have to be extracted and accelerated in order to form the ion beam. At the same time electrons must be removed from the beam in order to obtain high ion current and proper beam profile. If not, their charge increases the beam divergence and ion neutralization.

In ITER, the negative ions produced in the extraction zone have to be accelerated up to high energy, then they pass through the neutralization zone eventually reaching the fusion chamber. High energy accelerators are typically equipped with multi-stage grid systems that can handle voltages in the order of 1 MV. To limit the electrostatic repulsion between the accelerating ions, fine tuned elements called *Kerbs* are placed between the grids. They allow the electrostatic

focusing of the beam by tailoring the E-field equipotential lines.

As the design particle energy in NIO1 is only 60 keV, the grid system of NIO1 is composed by three elements, each with a central array of 3x3 apertures that defines the beam:

- the **plasma grid** (PG) divides the volume of the source from the beam vessel and its holes are accurately shaped to guarantee the best optics specifications. In order to prevent electron extraction, a recent upgrade allows to positively bias the PG (up to 20 V) with respect to the source body. Recently, an additional plate connected to the source body called Bias Plate was introduced in front of the PG to further reduce the electron density near the apertures. The PG can be charged up to -60 kV with respect to the ground.

- the **extraction grid** (EG) is the second electron barrier, it is charged at few kV above the PG and it is placed at the distance of 5 mm. In addition to the strong E-field between PG and EG, a vertical magnetic field is created by four permanent magnets that bend the electron trajectories until they collide with the EG itself because of the Lorentz force. In this way the majority of the electrons are taken apart from the beam because of their smaller mass. Their energy is transferred during the constant bombardment to the water cooled EG and their charge is given back to the source by using the regulated power supply.

- the **post acceleration grid** (PA) is placed 25 mm after the EG and it is kept at ground potential. PA gives the negative ions the main push. This time though, incoming velocity cannot be neglected and the ion trajectories are described by the equation presented in section 2. After the PA an additional repeller electrode prevents positive ions that can form at the end of the beam vessel from being accelerated back to the source.
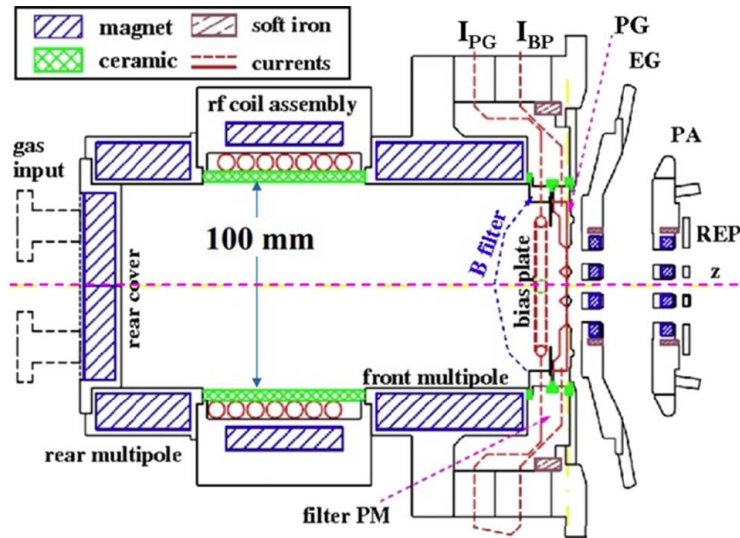

Figure 5: NIO1 source chamber and grids.

In the extraction zone near the PG, electric potential lines define a set of surfaces facing the apertures. The region that has the same potential of the source's walls is called *meniscus*, it has the shape of a convex lens and the thickness of less than 10 Debye length (about 2 mm).

1.5 The space charge

The space charge is an excess of electric charges distributed over a region of space, usually in vacuum. The discovery of this phenomenon dates back to the early years of '900 when, thanks to Richardson's studies, it was understood that thermionic emission is limited by the formation of a cloud of electrons around the hot cathode. Using classical notions of electrodynamics, he found that both the increasing in the temperature of the cathode and the enhancing of

the filament surface positively affects the maximum current limit in a fashion that resembles the Arrhenius equation, later called the "$T^{1/2}$ form". However, by 1928, further experimental discoveries with enhanced filaments and higher vacuum, proved classical theories to be wrong while the quantistic theory allowed to explain the enhancing mechanism and led Richardson to win the Nobel prize thanks to the law named after him:

$$J_R = A_0 \; T^2 \; \exp\left[\frac{-W}{kT}\right] \qquad [\text{A/m}^2] \tag{1}$$

In 1911 Child discovered that, beside cathode temperature, the accelerating field plays a critical role defining the emitted current. More precisely, he found that, for hot enough cathode, the maximum extracted ion current is proportional to the anode-to-cathode voltage to the power of 3/2 and proportional to the inverse square of the distance between the electrodes:

$$J_{\text{CL}} = \frac{4\varepsilon_0}{9d^2}\sqrt{\frac{2q}{m}}V_a^{3/2} \qquad [\text{A/m}^2] \tag{2}$$

This relation was later called Child-Langmuir (CL) limit current, because of independent studies by Langmuir on electron current in cylindrical valves.

Both laws are useful when it comes to predict the emission of hot cathodes: the current limit is defined as a function of the anode voltage by the smaller of the two. Increasing the voltage, the transition between Child's and Richardson's law occurs smoothly as the space charge changes its shape in the 3D space.
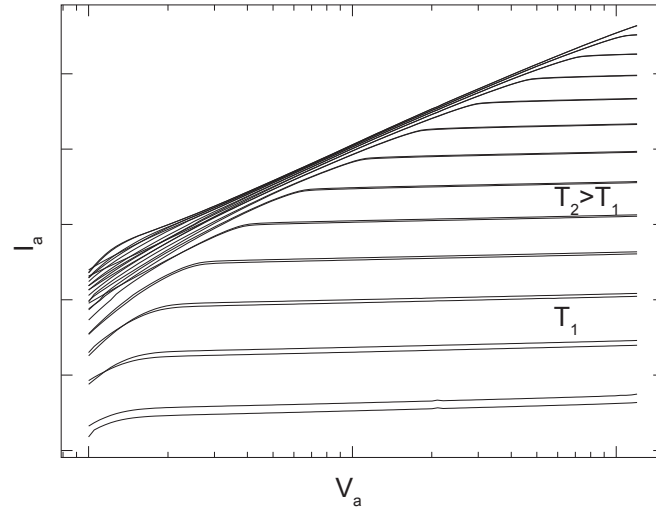

Figure 6: Hot cathode emitted current. At high voltages the Richardson law causes saturation because of the production emission deficiency, higher temperature allow more current. At low voltages, space charge accumulates near the filament limiting the emitted current.

In the following pages, Dushman formulation of Richardson's law and the classical derivation of Child-Langmuir current limit are presented. The following reference images are taken from [10].

Richardson's law

Let two planar metallic surfaces face each other at distance x in a vacuum chamber, if one of them is heated to sufficiently high temperature, some free electrons get enough energy to escape the potential barrier and leave the metal with an average velocity v_x normal to the surface.

The surface current density can be written as:

$$J_x = \int q \; n[E] \; v_x[E] \; dE \tag{3}$$

where $q = 1.6022 \times 10^{-19}$ C is the electron charge, $n[E]$ is the electron volumetric density for a single excitation state measured in J^{-1} m^{-3} and the integral is taken over all the electron energies needed for leaving the potential barrier in x direction. Density can be written as a two functions product: the states density $g[E]$ and $f[E]$ the probability for a given state with energy E. Fermi-Dirac statistics poses:

$$g[E] = 4\pi \frac{\sqrt{8m^3 E}}{h^3}$$

$$f[E] = \frac{1}{1 + \exp\left[\frac{E - E_F}{kT}\right]}$$

where h and k are the Planck's and Boltzmann's constants, E_F is the Fermi level that is the highest energy of electron in constant confining potential U. Only electrons with energies $E >> E_F$ can escape from the cathode. In this case $f[E]$ approaches the Maxwell-Boltzmann's distribution:
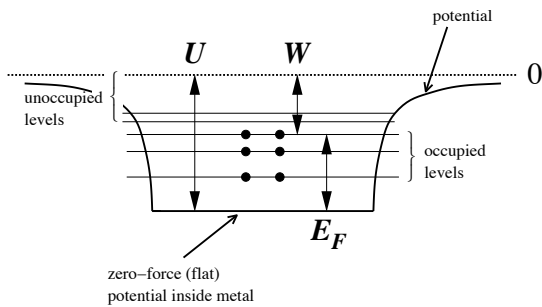
$$f[E] \simeq \exp\left[-\frac{E - E_F}{kT}\right]$$

If the electron kinetic energy is defined as E, it becomes possible to rewrite eq. (3) by replacing:

$$E = \frac{1}{2}mv^2 \quad \Rightarrow \quad \sqrt{E} \; dE = \frac{1}{\sqrt{2}}m^{3/2}v^2 \; dv \quad \Rightarrow \quad n[E] \; dE = \frac{8\pi m^3}{h^3}\exp\left[-\frac{E - E_F}{kT}\right]v^2 \; dv$$

$$J_x = \int q \; v_x[E] \; \frac{8\pi m^3}{h^3}\exp\left[-\frac{E - E_F}{kT}\right]v^2 \; dv$$

$$= q \; \frac{2m^3}{h^3} \; \exp\left[\frac{E_F}{kT}\right]\int v_x[E] \; \exp\left[\frac{-E}{kT}\right]4\pi v^2 \; dv$$

(a) Valence electrons inside the cathode fill all the free states over the Fermi level. Bounding electrons with maximum energy need exactly W in order to leave the metal and escape the mirror-image pull.
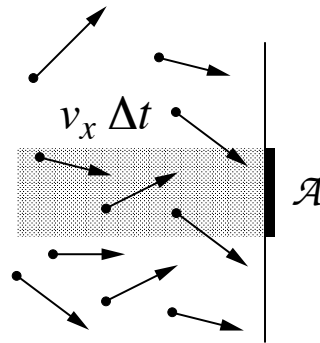
(b) Among the electrons with sufficient velocity v_x, all electrons in the shaded volume hit the surface $\mathcal{A}$ during Δt. Electrons with larger perpendicular velocity does not hit $\mathcal{A}$ but they are matched by ones in neighboring volumes.

Velocity can be divided in its three spatial components, the integral taken along the x direction starts from electrons at the Fermi level, $v = v_{x \text{ min}}$, while the integrals along the other directions extend at all velocity:

$$U = \frac{1}{2}mv_{x \text{ min}}^2 \Rightarrow v_{x \text{ min}} = \sqrt{\frac{2U}{m}}$$

$$J_x = \frac{2em^3}{h^3} \ \exp\left[\frac{E_F}{kT}\right] \int_{v_{x \text{ min}}}^{\infty} v_x \ \exp\left[\frac{-mv_x^2}{2kT}\right]dv_x \ \int_{-\infty}^{\infty} \exp\left[\frac{-mv_y^2}{2kT}\right]dv_y \ \int_{-\infty}^{\infty} \exp\left[\frac{-mv_z^2}{2kT}\right]dv_z$$

Those integrations can be easily computed by remembering the Gauss integral:
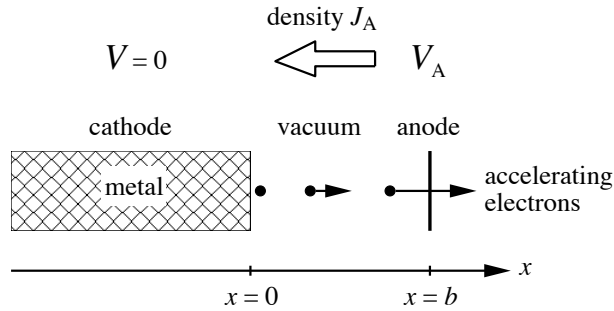
$$\int_{-\infty}^{\infty} \exp[-Cx^2] \ dx = \sqrt{\frac{\pi}{C}}$$

that finally leads to:

$$\begin{aligned} J_x &= \frac{2em^3}{h^3} \ \exp\left[\frac{E_F - U}{kT}\right]\frac{kT}{m}\sqrt{\frac{2\pi kT}{m}}\sqrt{\frac{2\pi kT}{m}} \\ &= \frac{4\pi emk^2}{h^3} \ T^2 \ \exp\left[\frac{E_F - U}{kT}\right] \\ &= A_0 \ T^2 \ \exp\left[\frac{-W}{kT}\right] \end{aligned} \qquad (4)$$

where $A_0 = 1.2 \times 10^6$ A/m^{2}K^2 is the Richardson's constant and W the characteristic work function of the cathode metal.

Child's law

Starting from the same planar interface used for the derivation of Richardson's law, one should know by now, that the space between $x = 0$ and $x = b$ is not really empty, instead it is populated by electrons that escape the cathode, forming a cloud with density n. If a voltage V_a between anode and cathode is applied, electrons are accelerated by this external electric field, creating a positive current J_A conventionally directed from anode to cathode, whose density is:

$$J_A = q \ n[x] \ v[x] = -J$$

Climbing the potential well electrons lose kinetic energy so, once they start to accelerate under the external field, their energy is almost zero. This is an important assumption, because in cases where the initial speed cannot be neglected[1] the current limit increases dramatically. For this example though, assuming the cathode temperature around 2000 K, the electrons have an average thermal energy near 0.3 eV that becomes small for anodic potential over few tens of

[1]This is the non-zero initial velocity CL law generalization shown in section 2.

Volt. Using the conservation of energy a second time, one can write the expression of their velocity as a function of the potential $V[x]$:

$$\frac{1}{2}mv^2 - qV[x] = 0 \quad \Rightarrow \quad v = \sqrt{\frac{2q}{m}V[x]}$$

Charge conservation in steady state assures that the current density does not depend on the position x, thus $n[x]$ must decrease as the electrons accelerate towards the anode. The space charge influences the potential following the Poisson's equation:

$$\frac{\partial^2 V[x]}{\partial x^2} = \frac{q\ n[x]}{\varepsilon_0} = \frac{J_A}{\varepsilon_0\sqrt{2qV[x]/m}} = a\ V^{-1/2}$$

In order to solve this second order differential equation, two boundary conditions are needed: the first one comes from fixing the cathode potential while the second one means that the charge density around the cathode is so high that the E-field in $x = 0$ becomes zero and no more current can be extracted:

$$V[0] = 0, \qquad \left.\frac{dV[x]}{dx}\right|_{x=0} = 0$$

The integration can be done by separation of variables:

$$\frac{dV[x]}{dx}\frac{d^2V[x]}{dx^2} = aV^{-1/2}\frac{dV[x]}{dx}$$

$$\int d\left[\frac{1}{2}\left(\frac{dV}{dx}\right)^2\right] = \int a\ V^{-1/2}\ dx$$

$$\frac{1}{2}\left(\frac{dV}{dx}\right)^2 = 2a\ V^{1/2} + c_1$$

integration constant c_1 must be zero because of the second boundary condition,

$$\int V^{-1/4}\ dV = \int \sqrt{4a}\ dx$$

$$V[x] = \left(\frac{3}{4}\sqrt{4a}\ x\right)^{4/3} + c_2$$

constant c_2 must also be null, as a result, the potential along x is written as:

$$V[x] = \left(\frac{9}{4}\frac{J_A}{\varepsilon_0\sqrt{2q/m}}\right)^{2/3}x^{4/3}$$

finally, calling the anodic voltage $V_A = V[b]$ and inverting the relation, leads to the Child's law:

$$J_A = \frac{4\varepsilon_0}{9b^2}\sqrt{\frac{2q}{m}}\ V_A^{3/2} \tag{5}$$

2   Parametric model description

The principal outcome of this work is a theoretical model of an interface similar to those seen in section 1.5. Instead of relying on the thermionic emission phenomenon, the present model assumes the presence of a generic source of electrical charges. Particles which are created at the beginning of the interface, can have initial kinetic energy, they are accelerated towards the end of the interface forming a particle beam which trajectory is mainly determined by the external E-field and the beam current intensity.

The proposed model is firstly introduced for a source capable of producing one type of particle, then it is generalized to a two particles source. Both of them are needed to accurately describe the extraction of the beam from the source and its acceleration.

Moreover, this model defines a current intensity limit that is the generalization of the classical CL law.

Due to the frequent use of partial derivatives in this section, the notation will be shorted as follows:

$$\frac{\partial^n}{\partial x^n}\left[f[x]\right] \ := \ \partial_x^n f[x]$$

2.1   Hypothesis

- The interface is monodimensional. The beam diameter is assumed to be small compared to its length, however this is not quite true for NIO1. Grids apertures have a diameter of 6 mm while the distance between the Plasma Grid and the Extraction Grid is only 5 mm. As a consequence, this model can't describe accurately the beam optics.

- Since the beam moves through E and B fields that are constant in time, Maxwell's equations are decoupled: $\nabla \times E = 0$, $\nabla \times B = \mu_0 J$.

- Magnetic field produced by the current of each beamlet is small compared to the external one that bends the trajectories of electrons: $B = B_{\text{ext}}$.

2.2   Adimensional formulation

An often used strategy, to maintain the widest approach to the subject, makes use of scaled variables. Following definitions are particularly useful also during numerical computations, because they remove precision issues that emerge from huge differences between fundamental constants of physics like the electron mass $m_e = 9.109 \times 10^{-31}$ kg or the vacuum permittivity $\varepsilon_0 = 8.854 \times 10^{-12}$ F/m. Hence for this section, all the equations are written in their adimensional form, unless otherwise specified.
As said earlier, this model is thought to be dependent on time and on one spatial dimension; from the following definition of this pair of parameters, important properties are derived:

- the scaled time dimension t is the sum of two terms: the simulation time s, and the delay τ. The time scaling factor is called T.

$$t = s + \tau$$

- the scaled spatial dimension is denoted by the letter x and its scale factor is L. d is the scaled distance between the two fixed voltage planes (or grids). More precisely, x defines the position of a particle that entered the domain at the time τ

$$x = f[s,\tau], \qquad x \in [0,d]$$

such strong condition allows to completely ignore the particles outside the domain.

Of course, all the variables of interest must be scaled accordingly in order to become adimensional. It is very important to point out that the sign of charges involved is, for the moment, positive. This choice may be confusing at first especially when the relation between E-field and the potential is used. However, it helps to keep the formulation as general as possible and, at the end, coming back to unscaled variables with proper electrical charge is a straightforward task.

Table 1: Scale factors. m and q are the particle's mass and (positive) electric charge.

scaled variable	symbol	factor
particle velocity	v	$\frac{L}{T}$
potential	V	$\frac{m}{q}\left(\frac{L}{T}\right)^2$
electric field	E	$\frac{m}{q}\frac{L}{T^2}$
charge density	ρ	$\frac{m}{q}\frac{\varepsilon_0}{T^2}\frac{1}{T^2}$
current density	J	$\frac{m}{q}\frac{\varepsilon_0}{T^3}\frac{L}{T^3}$

It will be showed that length scale factor L and time scale factor T can be of arbitrary magnitude as the mass and the charge of the particle. As a matter of fact, all the scale factors must cancel out when the equations are converted in physical dimensions if a very adimensional model is used.

2.3   Single particle model

From the differential form of Maxwell's equations, under the aforementioned hypothesis, it is possible to derive three fundamental relations:

$$\text{Electric charge conservation:} \quad \partial_t \rho - \partial_x J = 0$$
$$\text{Momentum conservation under E-field:} \quad \partial_t v + v\partial_x v = \partial_x V \tag{6}$$
$$\text{Poisson's equation / Gauss flux theorem:} \quad \partial_x^2 V = \rho$$

where the current density sign is due to the positive definition of the elementary charge used in this work. In addition to them, other well known relations are implicitly used to complete the model: electrostatics poses $\partial_x V = E$ and kinematics poses $\partial_t v = x$. The experimental conditions under investigation dictates the following Dirichlet boundary conditions:

$$\left.\begin{array}{r} v = v_0 \\ V = V_0 \\ \rho = \rho_0 \end{array}\right\} \quad \text{for } x = 0$$

$$V = 0 \qquad \text{for } x = d$$

Speaking of potentials, it is obvious that the meaningful value is the potential difference ΔV. In fact, a constant value can be summed to the function V when needed (e.g. figure 11).
Before starting the analysis, it might be useful to compute the differential of generic functions that depends on s and τ, in order to easily recall it when needed, in particular for x and t.

$$\nabla_{s\tau}\begin{bmatrix} t \\ x \end{bmatrix} = \begin{bmatrix} \partial_s t & \partial_s x \\ \partial_\tau t & \partial_\tau x \end{bmatrix} = \begin{bmatrix} 1 & v \\ 1 & * \end{bmatrix}$$

While three values of the derivatives in the table above, are quite obvious, one of them needs some further consideration. Due to the definition of x, all particles start at $x = 0$ at simulation time $s = 0$, whatever delay they have. In other words:

$$x[0, \tau] = 0 \quad \Rightarrow \quad \left.\partial_\tau x\right|_{s=0} = 0$$

For all the other (positive) values of s, the partial derivative of x versus τ remains implicit, due to the definition of x. This is not a problem because at least, when the ion beam is in a stationary state, $\partial_\tau = 0$ always. Of course this ceases to be true when the beam enters the instability zone, during transients and for some periodic solutions.

At this point, total derivative rules are applied to a generic function $f[x, t]$ in order to easily recall them when needed. Results are not obvious, instead they provide some hints to link together the three equations in (6).

$$\partial_s[f[x,t]] = \partial_x f \cdot \partial_s x + \partial_t f \cdot \partial_s t \quad \Rightarrow \quad \partial_s[\ ] = \partial_t[\ ] + v\partial_x[\ ]$$

$$\partial_\tau[f[x,t]] = \partial_x f \cdot \partial_\tau x + \partial_t f \cdot \partial_\tau t \quad \Rightarrow \quad \partial_\tau[\ ] = \partial_t[\ ] + (\partial_\tau x)\partial_x[\ ] \tag{7}$$

$$\partial_s[\ ] - v\partial_x[\ ] = \partial_\tau[\ ] - (\partial_\tau x)\partial_x[\ ] \quad \Rightarrow \quad \partial_x[\ ] = \frac{\partial_s[\ ] - \partial_\tau[\ ]}{v - \partial_\tau x}$$

Thanks to (6) and (7) a pattern becomes clear, in fact the main variables are linked together by derivative in x and s:

$$\begin{aligned}
\partial_x V &= E & \partial_s x &= v \\
\partial_x E &= \rho & \partial_s v &= E
\end{aligned} \tag{8}$$

In order to solve such system of equations one need to choose between the two variables, integrate all the derivatives chain, then apply the boundary conditions. A graphical representation of this algorithm can be seen in fig. 7. In this case, s is more convenient because if exists a generic function $f[t]$, 4 times derivable such that:

$$f''''[t] = f''''[s + \tau] = \partial_s E \tag{9}$$

then it is possible to write a convenient system of equations in t, in which each function is the integral over s of the previous one:

$$\begin{aligned}
E[s, \tau] &= f'''[s + \tau] + c_1[\tau] \\
v[s, \tau] &= f''[s + \tau] + c_2[\tau] + c_1[\tau]s \\
x[s, \tau] &= f'[s + \tau] - f'[\tau] + c_2[\tau]s + c_1[\tau]\frac{s^2}{2}
\end{aligned} \tag{10}$$

In the last one of (10) $c_3[\tau] = f'[\tau]$ because $x[0, \tau] = 0$ by definition. The other boundary conditions apply as follows:

$$\begin{aligned}
E[0, \tau] &= f'''[\tau] + c_1[\tau] = E_0[\tau] \\
v[0, \tau] &= f''[\tau] + c_2[\tau] = v_0[\tau] \\
x[0, \tau] &= f'[\tau] - f'[\tau] = 0
\end{aligned}$$

Functions c_1 and c_2 act respectively as E-field and initial speed variations during non-steady operations, they become zero whenever the boundary conditions match the initial conditions.

2.4 Steady-state solutions

One simple and handy solution of the system (10) is obtained when all the variables are independent from τ. So, as soon as the beam becomes steady, all the ∂_τ become zero and boundary conditions E_0, v_0 become constants. From the first of (6) it follows that:

$$\partial_x J = 0 \quad \Rightarrow \quad \partial_s J = 0$$

and from the third of (6) + (9) one can tell that:

$$\partial_s E = v \partial_x E = J$$

The last identity allows to close the circle seen in (8) so the system (10) can be rewritten and completed with the final set of equations:

$$
\begin{aligned}
J[s] &= J_0 \\
E[s] &= E_0 + J_0\ s \\
v[s] &= v_0 + E_0\ s + J_0 \frac{s^2}{2} \\
x[s] &= v_0\ s + E_0 \frac{s^2}{2} + J_0 \frac{s^3}{6} \\
V[s] &= \frac{1}{2}\left(v[s]^2 - v_0^2 \right) \\
\rho[s] &= J[s]/v[s]
\end{aligned}
\tag{11}
$$

A graphical representation of how the model solution is computed is given in fig. 7, please note that since the model is parametric in s, all the integrations are computationally inexpensive. Moreover, when the relation between different variables e.g. (extraction current versus extraction voltage) has to be showed, the system of parametric functions allows to plot the desired chart at once. The list of parametric charts in section 2.8 is only one example of the flexibility of this approach.
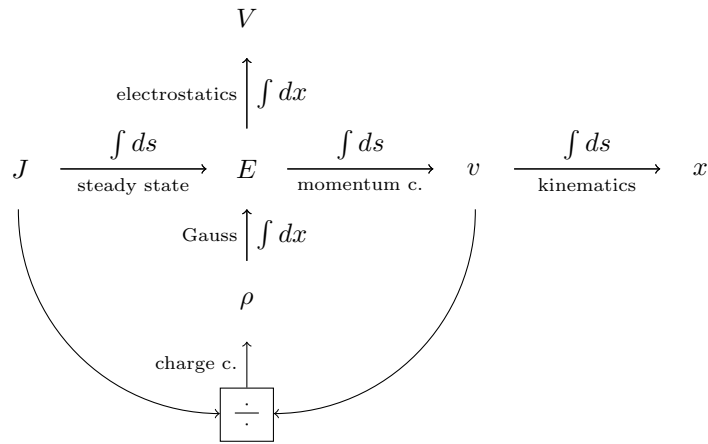

Figure 7: Steady-state single particle model scheme. Connections between the variables are made possible thanks to the well known physics principles recalled in (6).

2.5 Child-Langmuir current limit generalization

Steady state equations allow infinite solutions (∞^3); fixing the values of grid voltages and incoming particle velocity, leads to a unique solution $J = J_{\max}$. In order to find the explicit function of $J_{\max}$, one has to find first the relation between E_0 and v_0. In other words, everything comes down to a conversion from a Dirichlet to a Neumann boundary condition.
If s_d is the simulation time needed for every particle to reach d,

$$x[s_d] = d$$

both the position and the potential in d can be written as:

$$x[s_d] = v_0 s_d + E_0 \frac{s_d^2}{2} + J_0 \frac{s_d^3}{6} = d$$

$$V[s_d] = V_d = \frac{1}{2}\left(v[s_d]^2 - v_0^2\right) = \frac{1}{2}\left(\left(v_0 + E_0 s_d + \frac{1}{2}J_0 s_d^2\right)^2 - v_0^2\right)$$

The $J = J_{\max}$ condition can be seen from different perspectives, in fact it is equivalent to $V_d = V_{d,\min}$. This minimum can be found by deriving V_d by E_0 once the $\partial_{E_0} s_d$ is known. Help comes once again from $x[s_d]$ expression, as:

$$\partial_{E_0} x[s_d] = v_0 \partial_{E_0} s_d + \frac{s_d^2}{2} + E_0 s_d \partial_{E_0} s_d + J_0 \frac{s_d^2}{2}\partial_{E_0} s_d = 0$$

$$\Rightarrow \partial_{E_0} s_d = -\frac{s_d^2}{2}\frac{1}{v[s_d]}$$

$$\begin{aligned}
\partial_{E_0} V_d &= \left(v_0 + E_0 s_d + \frac{1}{2}J_0 s_d^2\right)\left(s_d + E_0 \partial_{E_0} s_d + J_0 s_d \partial_{E_0} s_d\right)\\
&= v[s_d]\left(s_d - E_0 \frac{s_d^2}{2}\frac{1}{v[s_d]} - J_0 \frac{s_d^3}{2}\frac{1}{v[s_d]}\right)\\
&= s_d\left(v[s_d] - E_0 \frac{s_d}{2} - J_0 \frac{s_d^2}{2}\right)\\
&= s_d\left(v_0 + E_0 \frac{s_d}{2}\right)
\end{aligned}$$

Finally, steady state V_d minimum is found when $\partial_{E_0} V_d = 0$. After some substitutions, this leads to the definition of four limit conditions which are mutually exclusive:

$$\begin{aligned}
E_{0,\max} &= -\frac{2v_0}{s_d}\\
s_{d,\min} &= \sqrt[3]{\frac{6d}{J_0}}\\
V_{d,\min} &= -\frac{1}{2}v_0 \sqrt[3]{36d^2 J_0} + \frac{1}{8}\left(36d^2 J_0\right)^{2/3}\\
J_{\max} &= \frac{2}{9d^2}\left(v_0 + \sqrt{v_0^2 + 2V_d}\right)^3
\end{aligned} \tag{12}$$

Due to the sole degree of freedom left from the system (11), one can choose to maximize or minimize only one of this four parameters. The last one in particular, is the CL limit modified by the initial velocity. The earliest reference to a similar result is the historical article by G. Jaffé [11], where the normalized initial kinetic energy and the normalized distance between the electrodes determine the current limit. A more recent but non adimensional approach to this generalization can be found in [12]. If the physical units form of the generalized CL limit is required, the expression in (11) must be rewritten as follows:

$$J_{\max[\mathrm{SI}]} = \frac{2J_{\mathrm{scale}}}{9(d_{[\mathrm{SI}]}/L)^2}\left(\frac{v_{0[\mathrm{SI}]}}{v_{\mathrm{scale}}} + \sqrt{\left(\frac{v_{0[\mathrm{SI}]}}{v_{\mathrm{scale}}}\right)^2 + 2\frac{V_{d[\mathrm{SI}]}}{V_{\mathrm{scale}}}}\right)^3 \qquad \mathrm{A/m^2}$$

Of course, all the variables inside the expression are reduced with appropriate scale factors. Length scale L and time scale T cancel out during substitutions so they can be considered unitary.

2.6   Non steady solutions

As pointed out in [12], the analytical solution of the differential equation system becomes a formidable task. Even though numerical simulations can be performed using the time dependent equations showed in 10, it seems that the results are not as useful as the steady state ones, at least for the NIO1 experiment.

Further works may be focused on the study of pulsating beam that can, in principle, achieve a transient extracted current greater than the extended CL limit due to the lack of space charge in front of the pulse.

2.7   Extension of the CL law to simultaneous presence of electrons and ions

In accelerators such as NIO1 and SPIDER, negative ions are accelerated, so that negative ions and electrons are extracted through the PG and, between the first two grids, they define the combined total current. On the other hand, the initial velocity of the particles is almost zero: in NIO1 initial energy at the PG is less than 10 eV while, near the EG, particles have gained up to 8 keV. In the proximity of the PG, the space charge heavily affects the potential thus limiting the maximum current of the entire series of grids. After EG, most of the electrons have been eliminated from the beam and the current is made only by fast moving ions.

In this section, the presence of two different particles is studied in detail and an analytic model capable of finding the maximum current density is presented. The formulation of this extended model is similar to that of the single particle model in steady state: it is still adimensional and parametric, but one crucial difference is the definition of the spatial dimension parameter x.

As the mass influences the acceleration under the E-field, two different particles follow different trajectories hence the speed and the density must be computed separately. In the following equations, subscript i will be used for ions while e stands for electrons. This assumptions help keeping the formulation clear but they aren't needed in order to carry on the computations. In addition to that, trajectory of ions are selected to be the reference one, meaning that the variables v, x, ρ regarding ions, take the role of the ones used in the single particle model, while the electrons variables are calculated as functions of the former. Considering instead the other particle as the reference one, would have a negative impact on numerical stability because of the three orders of magnitude between m_i and m_e.

The two species constantly interact with each other so they are energetically bond while moving inside the same E-field. Calling $\gamma = \gamma_i/\gamma_e$ the ratio between ion and electron densities, such that $\gamma_i + \gamma_e = 1$, allows to write the electric potential as the superposition of two potentials:

$$\begin{aligned} V[x] = V_i[x] + V_e[x] &= V[x](\gamma_i + \gamma_e) \\ &= \frac{1}{2\gamma_i}(v_i[x]^2 - v_{i0}^2) \end{aligned} \tag{13}$$

It is important to note that the properties of the beam, like its charge density, can be separated in two components only if they are defined as functions of space, (summing two charge densities pertaining to different times would be absurd). In particular, position, speed and the density must be rewritten starting from eq. (13).

$$(v_i^2[x] - v_{i0}^2)\frac{m_i}{\gamma_i} = (v_e^2[x] - v_{e0}^2)\frac{m_e}{\gamma_e}$$

As seen in system (11) v_i is a parabola, so $v_i[x]$ has, in general, a critical point corresponding to the minimum where its slope changes sign. For this reason, in the most general case, $v_i[x]$ is defined by two cases: the decelerating arm and the accelerating arm. However, if both the initial velocities are zero $v_i[s]$ and $v_e[s]$ are monotonically growing so there is only one solution for their x-defined counterpart and it is easier to define them.

$$v_e[x] = v_i[x] \sqrt{\frac{\gamma_e\ m_i}{\gamma_i\ m_e}} \sqrt{1 - \frac{1}{v_i^2[x]}(v_{i0}^2 - v_{e0}^2 \frac{\gamma_i\ m_e}{\gamma_e\ m_i})}$$

$$\simeq v_i[x] \sqrt{\frac{\gamma_e\ m_i}{\gamma_i\ m_e}} \left(1 - \frac{1}{2v_i^2[x]}(v_{i0}^2 - v_{e0}^2 \frac{\gamma_i\ m_e}{\gamma_e\ m_i})\right)$$

The last expression can be verified only under the hypothesis of small initial velocities, thanks to the Mclaurin expansion truncated at the first element. If $v_{i0} = v_{e0} = v_0 = 0$ however, the expression becomes handy and can be easily used in density computations:

$$\left.\frac{v_i[x]}{v_e[x]}\right|_{v_0=0} = \sqrt{\frac{\gamma_e\ m_i}{\gamma_i\ m_e}} \tag{14}$$

As a result, the steady-state system (11) can be modified as follows:

$$\begin{aligned}
J[s] &= J_0 \\
E[s] &= E_0 + J_0\ s \\
x_i[s] &= v_{i0}\ s + \gamma_i E_0 \frac{s^2}{2} + \gamma_i J_0 \frac{s^3}{6} \\
V[x] &= \frac{1}{2\gamma_i}\left(v_i[x]^2 - v_{i0}^2\right) \\
\rho[x] &= J_0 \frac{\gamma_e}{v_i[x]}\left(\frac{v_i[x]}{v_e[x]} + \frac{\gamma_i}{\gamma_e}\right)
\end{aligned} \tag{15}$$

Differently from the single particle model, one other step is needed before doing further computations. The inverse expression of $x_i[s]$ must be found in order to change the parametrization of functions: $v_i[s]$ to $v_i[x_i]$ and $J[s]$ to $J[x_i]$. As functions of space, these quantities can be used to calculate the two densities, the electron velocity and lastly, the potential. Judging by the $x_i[s]$ expression, the inverse function can be found analytically, unless $J > J_{\max}$ it has a single solution. However, due to the large number of terms of its expression the inverse is automatically found with the `InverseFunction` Mathematica command and it is not shown here.

In synthesis, the algorithm followed to solve the system is graphically represented in the scheme of figure 8.

Four limit conditions found can be derived also for the two particle model taking into account the fraction γ_i. These expressions are important for their practical utility during experimental operations and also during the design phase because they define the maximum ratings of the particle accelerator. The modified expressions can be derived using those in (12) as a reference and equations from system (15):

$$\begin{aligned}
E_{0,\max} &= -\frac{2v_{i0}}{\gamma_i\ s_d} \\
s_{\mathrm{d,min}} &= \sqrt[3]{\frac{6d}{J_0\ \gamma_i}} \\
V_{\mathrm{d,min}} &= -\frac{1}{2\gamma_i} v_{i0} \sqrt[3]{36d^2 J_0} + \frac{1}{8\gamma_i}\left(36d^2 J_0\right)^{2/3} \\
J_{\max} &= \frac{2}{\gamma_i\ 9d^2}\left(v_{i0} + \sqrt{v_{i0}^2 + 2\gamma_i\ V_d}\right)^3
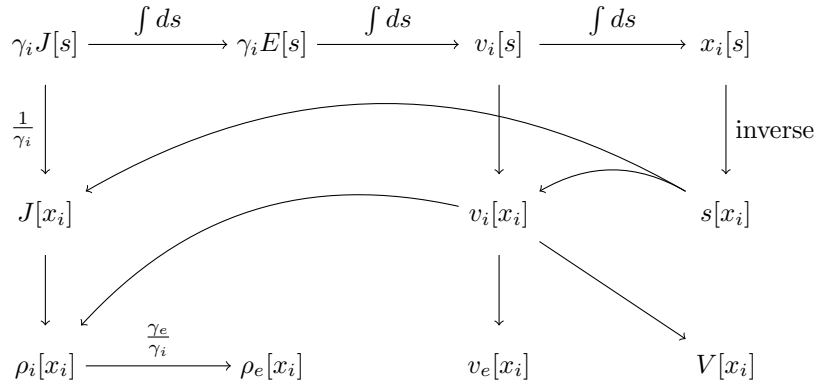\end{aligned} \tag{16}$$

Figure 8: Steady-state two particles model scheme. The increment in complexity compared to fig. 7 is mainly due to the inverse function.

The last expression is the two particles CL law generalization. The formulation in physical units is obtained as before:

$$J_{\max[\mathrm{SI}]} = \frac{2J_{\mathrm{scale}}}{9\gamma_i(d_{[\mathrm{SI}]}/L)^2} \left(\frac{v_{0[\mathrm{SI}]}}{v_{\mathrm{scale}}} + \sqrt{\left(\frac{v_{0[\mathrm{SI}]}}{v_{\mathrm{scale}}}\right)^2 + 2\gamma_i \frac{V_{d[\mathrm{SI}]}}{V_{\mathrm{scale}}}} \right)^3 \qquad \mathrm{A/m}^2$$

2.8   Parametric characteristics

The single particle model (SPM) and the two particles model (TPM) were analytically solved in section 2.4 and 2.7. In this section their graphical representation is made possible thanks to a Mathematica code, which can natively manage arrays of parametric expressions. All the code written for this thesis can be found in the appendix. In particular, each group of charts completely describe the beam characteristic variables (V, E, v, ρ, J) along the distance between the two grids, in a very wide range of possible situations.

SPM

- The SPM is firstly shown in figure 9 for $v_0 = 0$ meaning that the initial energy of the particles is zero, as in the classical CL law. The extraction voltage is parametrized as

$$V_{\mathrm{GE}} = 0.1 \; i^2$$

  where $i = \{1, \ 2, \ldots, \ 8\}$, in order to obtain better spaced lines. Potential, E-field, speed and density are monotonic functions and for each i, they are multiplied by a specific constant that can be easily calculated from (12). The bottom left chart of figure 9 shows the relation between the normalized simulation time and the position of a particle. The 8 lines are, not surprisingly, stacked together because both axes are normalized.

- The SPM is then shown in fig. 10 in its adimensional form at different extraction voltages

$$V_{\mathrm{GE}} = -1.387 + (0.35 \; i)!$$

In this way a family of curves describes four cases where the external E-field is braking incoming particles and other four cases in which particles are eventually accelerated. A necessary condition is, of course, $v_0 > 0$, which means that some initial kinetic energy can be spent against either the external E-field or the space charge E-field. As a result, the formation of a virtual cathode happens at a distance $x = x_{\mathrm{VC}}$ inversely proportional to the limit current. E-field starts negative and grows monotonically crossing zero at x_{VC}. At the same distance, velocity have their minimum and charge density has its maximum. The bottom left chart of figure 10 shows the relation between the normalized simulation time and the position of a particle. This time the lines are not staked because trajectories are non-linearly dependent on v_0.

- The SPM shown in fig. 11 is finally applied on hydrogen ions at different extraction voltages:

$$V_{\mathrm{GE}} = 250 \; i/\mathrm{Vscale}$$

In this way, a family of curves describes the particle acceleration under 8 different external E-field. To give results in physical dimensions, scale factors are applied to each variable. These are the factors listed in table 1, The transformation must also take into account the sign of the fundamental charge.
The initial speed selected for this example allows to extract a high H^- current, much more than the $v_0 = 0$ case. As in figure 10, the space charge forms a virtual cathode at a distance x_{VC} from the PG that increases as the extraction voltage decreases. An approximate value of the maximum current that can be extracted through the nine 6 mm apertures of the NIO1 grids, can be obtained by multiplying the value of the last curve in the bottom right chart by the total section:

$$500 \; \mathrm{A/m}^2 \cdot 9\pi \cdot 0.003^2 \; \mathrm{m}^2 \simeq 0.127 \; \mathrm{A}$$

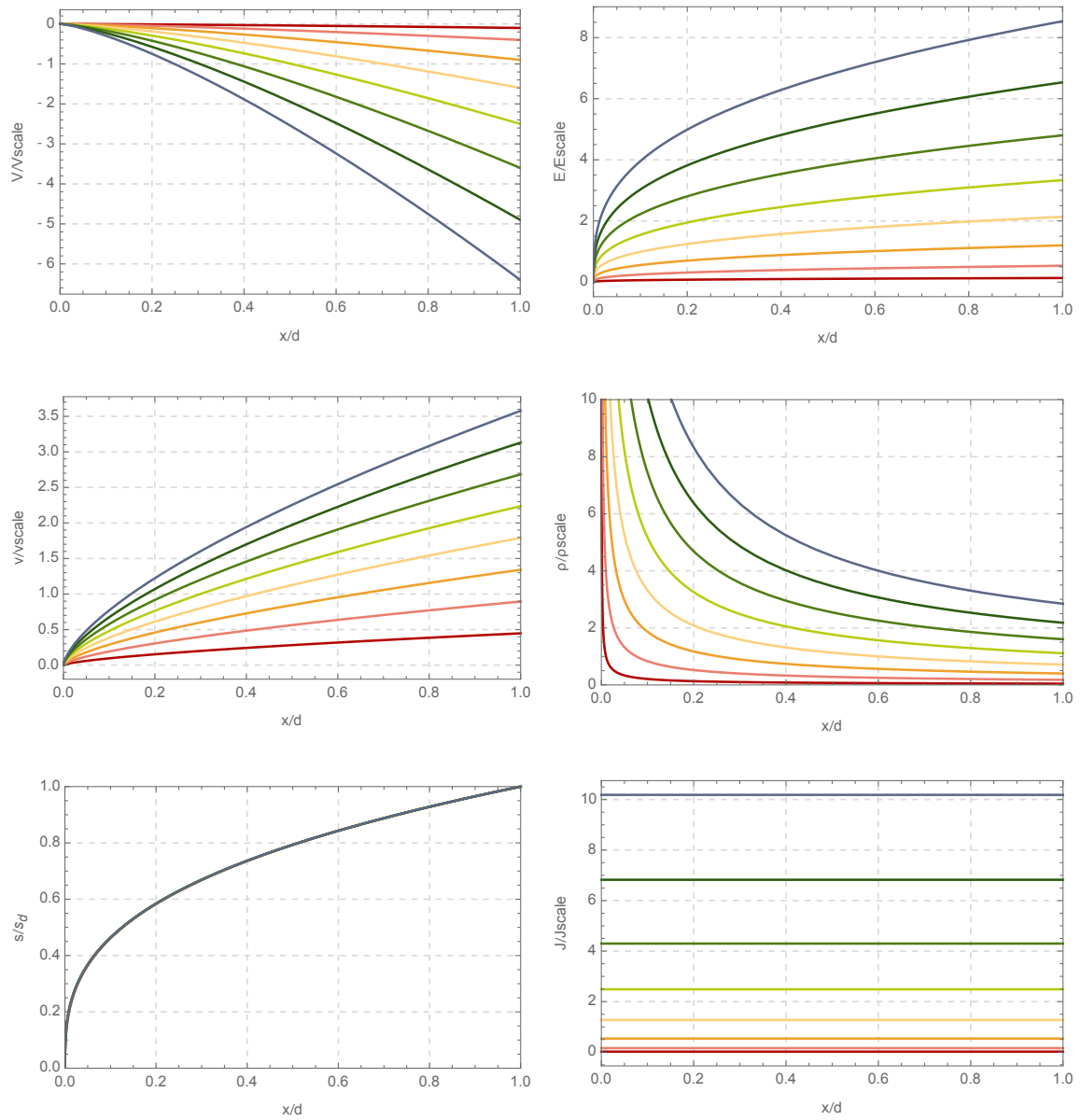that is very close to the nominal value of 130 mA.

Figure 9: Some adimensional SPM characteristics as the voltage between the grids increases. This is the $v_0 = 0$ case.
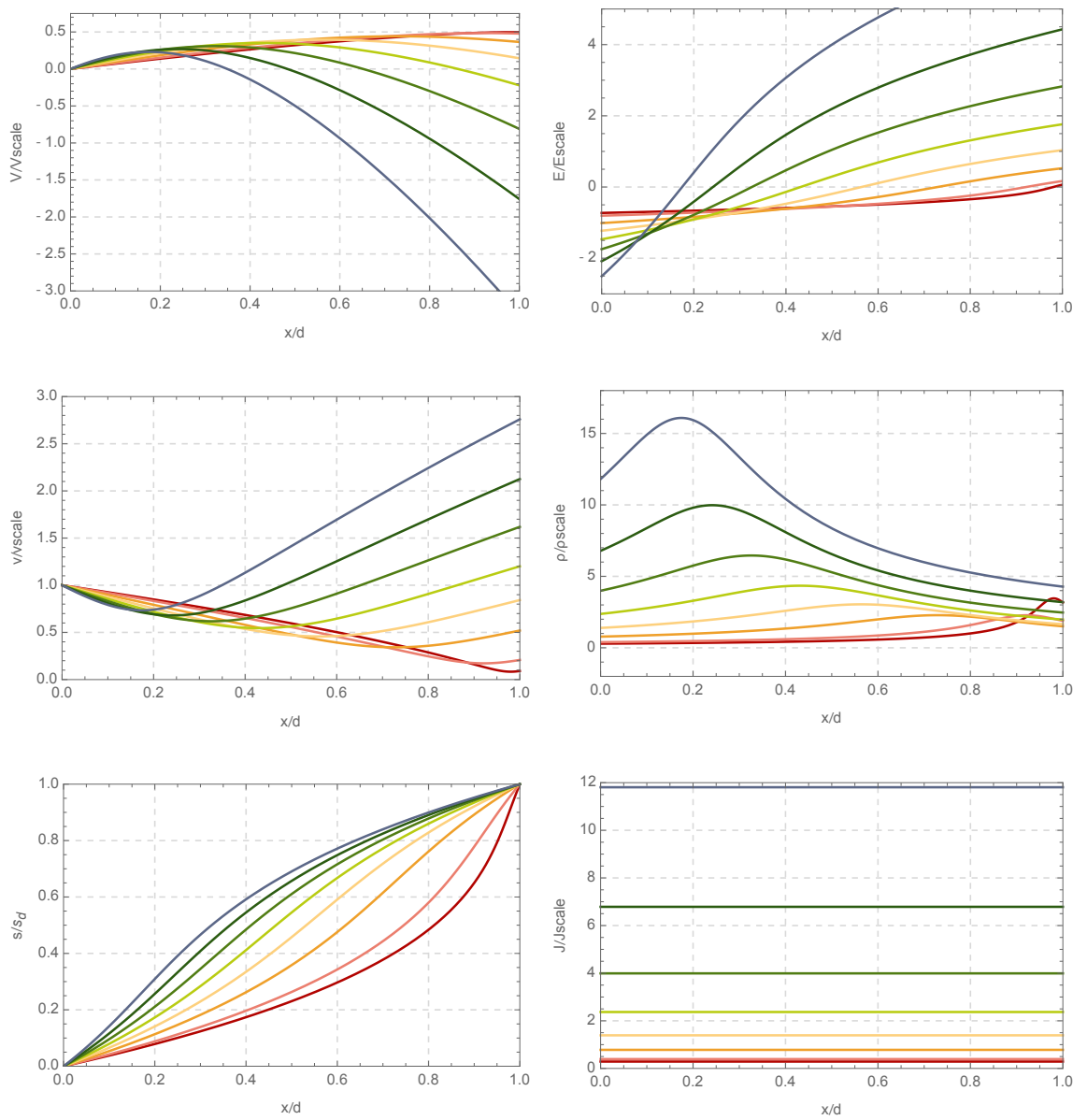
Figure 10: Some adimensional SPM characteristics as the voltage between the grids increases. This is the $v_0 > 0$ case.
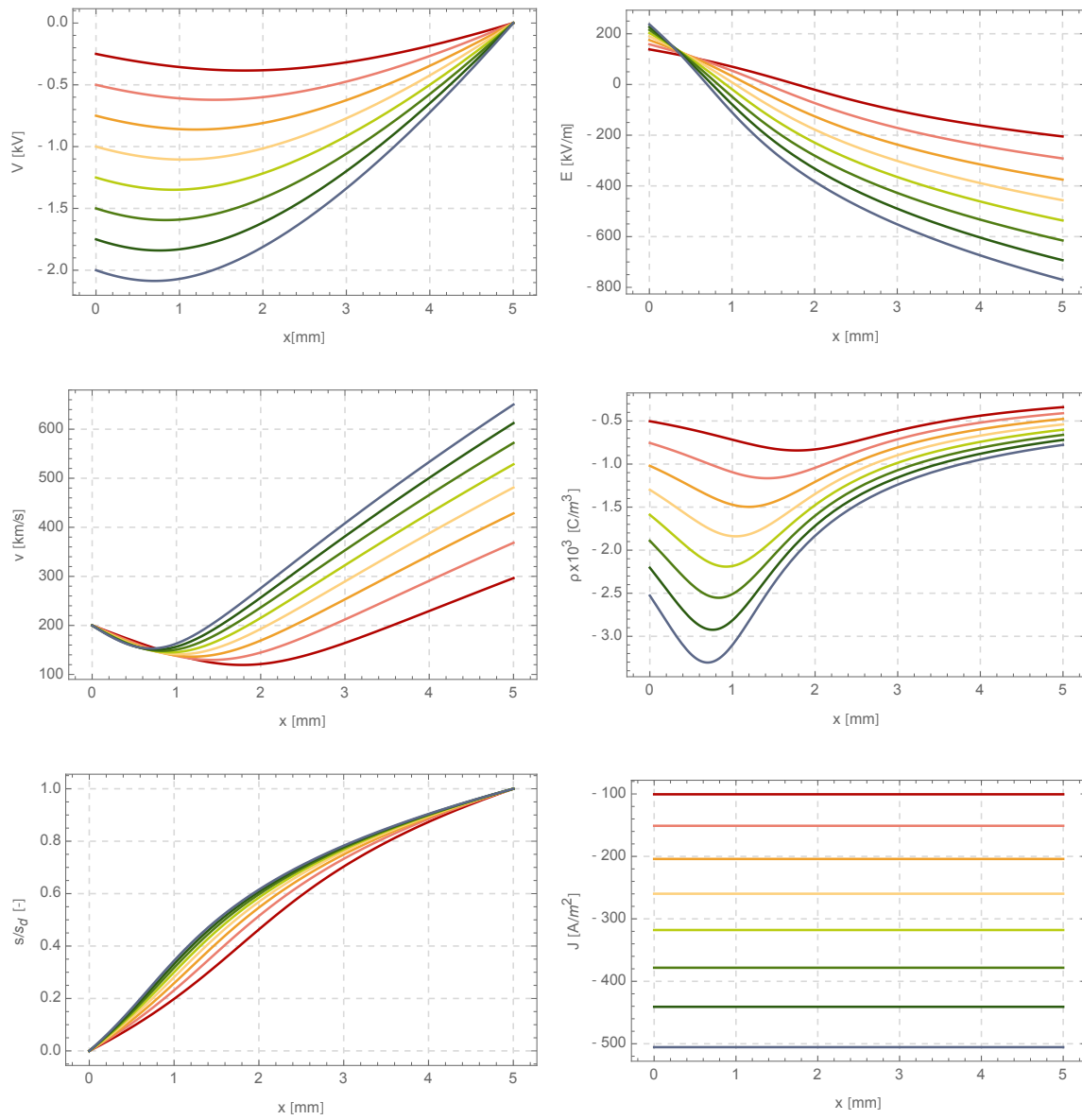
Figure 11: Some characteristics in SI units for hydrogen ions with $v_0 > 0$ as the voltage between the grids increases. Note that the fundamental charge here has its negative sign, in fact the potential is increasing with x and $J < 0$.

TPM

- Firstly, the TPM is introduced in figure 12 for $v_0 = 0$ meaning both the initial particles velocity are zero. Instead of varying the extraction voltage, 9 curves are obtained with the parametrization of the ratio between ion and electrons:

$$\gamma_i = i/10, \qquad i = \{1, \ 2, \ldots, \ 9\}$$

This is made in order to focus the reader's attention on the effects of a higher ion production capability of the source. In this example, the extraction voltage is fixed at 2000 V, a typical value used for the V_{GE} in NIO1.

While potential, E-field, simulation time and current density are variables of the whole beam, velocity and density are specific for ions and electrons, so they require two additional charts.

The first important feature that can be seen from this example is that both the potential and the E-field profiles do not change by varying γ_i. This was expected because of the proportionality already discussed in figure 9. As a consequence, all the velocity and density profiles are familiar with the exception of the logarithmic scale.

One new feature can be seen in the electron density chart where half the lines are stacked: for high ion density (blue line) ρ_e is small because the majority of the current is represented by ρ_i. As the ion density decreases, the electron density increases until it reaches a maximum (light-green line) after that it returns to precedent values.

The simulation time s has a chart similar to that in fig. 9. The last chart verifies that the current density limit is proportional to $\sqrt{\gamma_i}$ as seen in eq. (16).

- Lastly, figure 13 represents the TPM under the most complex condition: a beam made of H^- ions and electrons, each with proper initial velocity.

The applied extraction voltage is 2 kV as before, while the initial velocity, hence the energy, of the ions is fixed at 20 km/s. Although this value is unrealistically high for NIO1, it allows to see all the features of this figure without stacking. The parametrization in γ_i is almost the same as before with the exception of potential, E-field and simulation time charts where only odds i curves are displayed. This is done to distinguish different curves in close proximity.

The electron initial velocity is found as a consequence of the energy consideration discussed for eq. 14:

$$v_{e0} = v_{i0} \sqrt{\frac{\gamma_e \ m_i}{\gamma_i \ m_e}}$$

The main differences between fig. 13 and fig. 12 regards the smoothed charge density peak near the cathode and the increased current limit, both caused by the initial velocity. The current density chart of electrons shows features of fig. 11 and fig. 12 combined. Potential, E-field and simulation time charts show little deviations from the central curve because the initial speed is not (proportionally) as big as it is in fig. 11. In particular, the E-field profile is much less deformed because of the lower amount of initial kinetic energy that can be spent against the space charge field braking force.
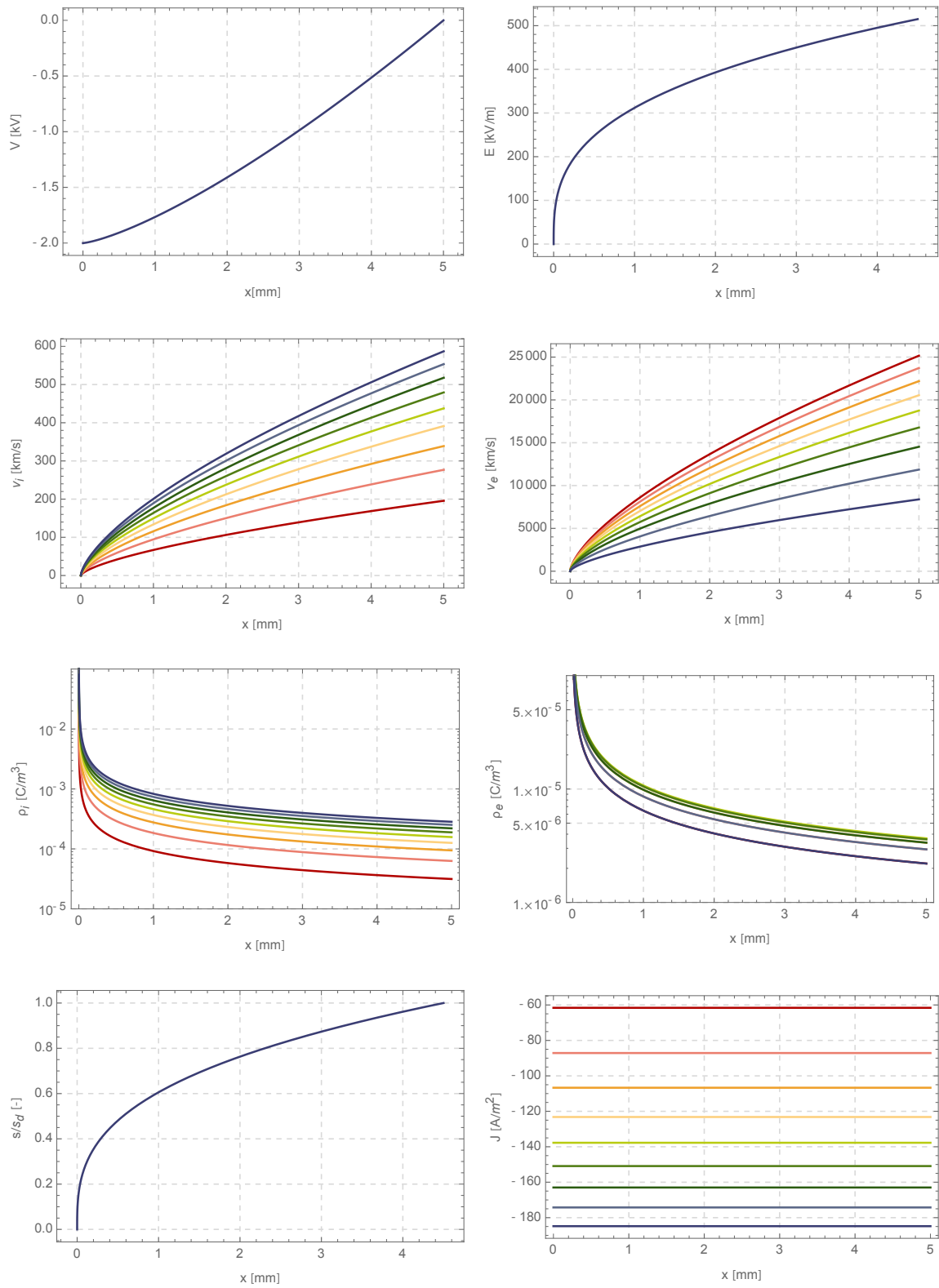
Figure 12: Some characteristics as the fraction γ_i of ions increases from 0.1 to 0.9.
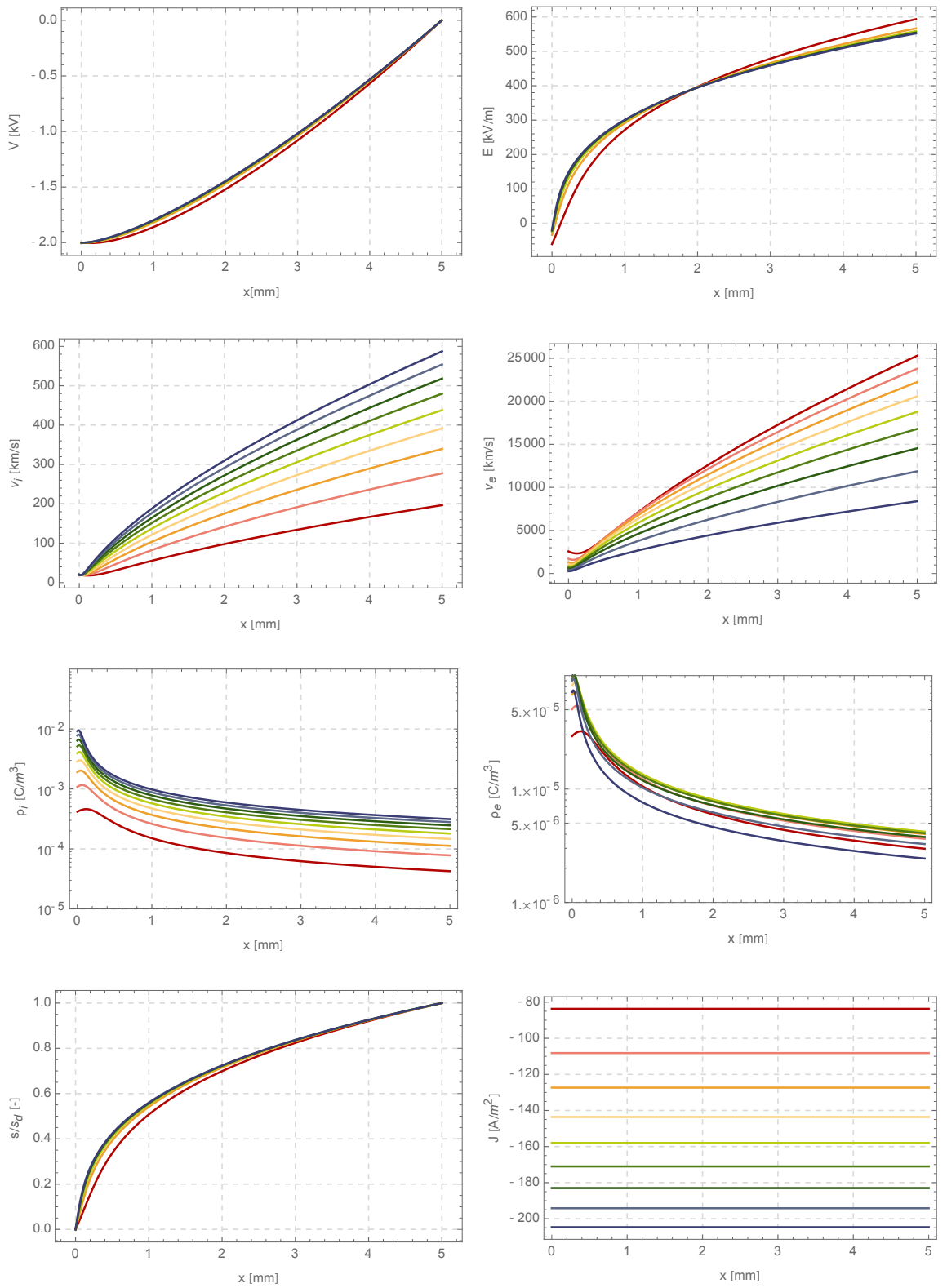This is the $v_0 = 0$ case.

Figure 13: Some characteristics as the fraction γ_i of ions increases from 0.1 to 0.9. This is the $v_0 \neq 0$ case.

Initial speed scan

One last example of what the parametric model is capable of regards the effect of the initial speed on the current limit. In this case, the maximum hydrogen ions current is calculated as a function of the extraction voltage by varying the initial ion velocity for a discrete number of values:

$$v_{io} = \{0, 10^4, 3 \times 10^4, 5 \times 10^4\}$$

The extraction of hydrogen from the source of the NIO1 experiment, is best described if the TPM is used. By doing so, one additional parameter, the fraction γ_i can be expressed. To date, the experimental data show that γ_i is very low, mainly because the caesium surface production cannot be used jet. The selected value for the following simulation is $\gamma_i = 0.25$.
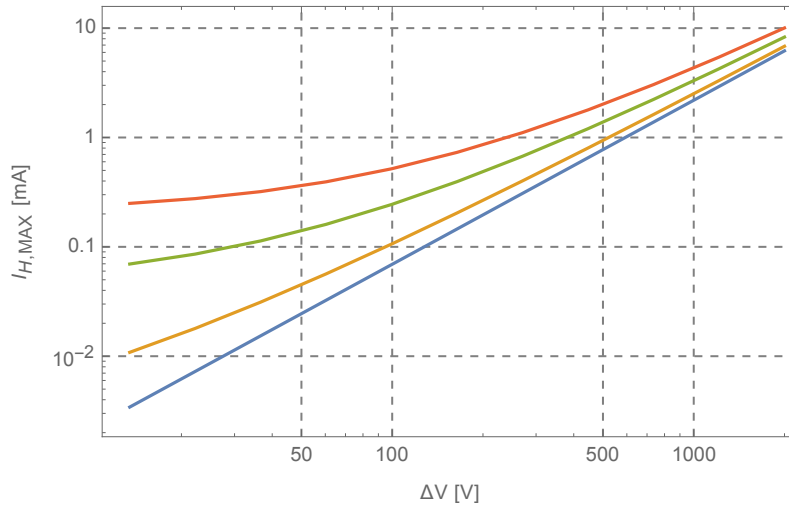

Figure 14: Effect of the initial speed on the current limit for hydrogen. The lower line represents the zero initial velocity case.

As the $V^{3/2}$ CL law is a straight line in logarithmic scale, figure 14 shows that the hydrogen ion current deviates from the $v_0 = 0$ curve as the initial speed is increased.

The current density is obtained again by multiplying the current density J by the total surface of the grid apertures of NIO1.

3 Experimental data of NIO1

At Consorzio RFX, where the NIO1 experiment is located, a database is updated at every acquisition session, recording nearly 70 parameters simultaneously. Every session is described in a diary, along with changes in functionalities, parts of the apparatus and suggestions for further improvements. This procedure allows to distinguish between datasets with different operation conditions. The datas used in this sections come from a restriction of the dataset, where parameter external to the model presented in section 2 are constants, e.g. the bias plate voltage or the vessel pressure.

Unfortunately, an instruments that can measure all the variables as shown in the charts of section 2.8 does not exists. The distance between PG and EG is only 5 mm and any physical probe would interfere with the plasma properties distorting the measurements.
However, NIO1 electrical parameters as grid voltages, currents and electric power can be monitored and varied with precision, their error is about 1%. In this section, the extraction grid voltage V_{EG}, called also extraction voltage, is the most important parameter: all the following charts are plotted with said abscissa.

3.1 Perveance

It is common, in the letterature of this field, to find an empirical parameter called perveance. It relates the beam current to the theoretical maximum defined by the classical CL law. Multiplying eq. (5) by the surface S defined by the apertures the expression becomes:

$$I_{\mathrm{CL}} \; = \; \frac{4S\varepsilon_0}{9d^2}\sqrt{\frac{2q}{m}} \; V_{\mathrm{ext}}^{3/2} \; = \; \Pi_{\mathrm{CL}} \; V_{\mathrm{ext}}^{3/2} \quad [\mathrm{A}] \tag{17}$$

the proportionality constant Π_{CL} is the maximum permeance value, it depends on the experiment geometry and the particle mass and charge. If the current found is lower than the CL limit, the ratio between the perveance of the beam and Π_{CL} is called normalized perveance:

$$\Pi = \frac{I_{\mathrm{ext}}}{V_{\mathrm{ext}}^{3/2}}, \qquad \pi = \frac{\Pi}{\Pi_{\mathrm{CL}}}$$

The definition of the perveance can be used to roughly estimate the ratio between CL limit currents for different ions, e.g. the comparison of hydrogen and oxygen tells:

$$\frac{\Pi_{\mathrm{CL,H}}}{\Pi_{\mathrm{CL,O}}} = \sqrt{\frac{m_O}{m_H}} \simeq 4$$

Unfortunately, what has been just found is not empirically verified, in most of the cases, for different reasons:

- all negative ion sources extract a current composed by both ions and electrons, the perveance computation cannot be made exclusively on ion current;

- different ions have different electronegativity, this has an impact on the optics of the beam and on the maximum γ_i obtainable.

To obtain a better agreement with the experimental values the TPM should be applied instead of classical CL in the definition of the permeance. If so, the ratio between the two perveances becomes:

$$\frac{\Pi_{\mathrm{TPM,H}}}{\Pi_{\mathrm{TPM,O}}} = \sqrt{\frac{m_O \gamma_H}{\gamma_O m_H}}$$

Three cases in which the beamlet is affected by the source parameters and the grid system parameters are shown in figure 15. The best perveance is the value for which the beam width is at a minimum. The other two situations in which the beam optics is far from the optimum

are called under-perveant and over-perveant with the perveance value lower and larger than the best perveance value respectively. The best perveance is always less than or equal the maximum perveance.
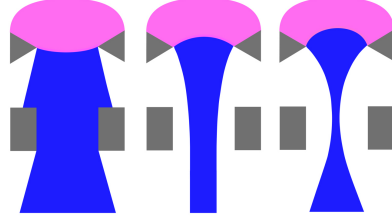

Figure 15: Beam optics: from the left the over-perveant beam, the optimal beam and the under-perveant beam. The meniscus can be find at the boundary between the colored areas.

3.2   Extraction voltage scans

To date, the NIO1 experimental apparatus operated only with hydrogen and oxygen. Although the ITER neutral beam injector will work with deuterium ions, the difference in performance between the two isotopes is too small to be addressed here.

Hydrogen operations

Experimental evidences from NIO1 show that the H^- extracted current follows CL limit only up to $V_{GE} = 0.5$ kV at 1 kW RF power, after that, saturation occurs and the perveance decreases. The physical reason behind the saturation phenomenon will be addressed in the last section. The electron current, extracted and collected on the EG, follows almost the same trend however it is remarkably higher. In the zone fitted with the CL law, the hydrogen ion fraction is approximatively:

$$\gamma_{iH} = 1.17\%$$

Most of the hydrogen extraction scans were performed at the fixed input power of 1 kW, in order to avoid source damages the pyrex insulator breakdown happened on May 2016. These operations were generally performed at higher pressure with respect to oxygen gas, so a direct comparison is not completely possible.
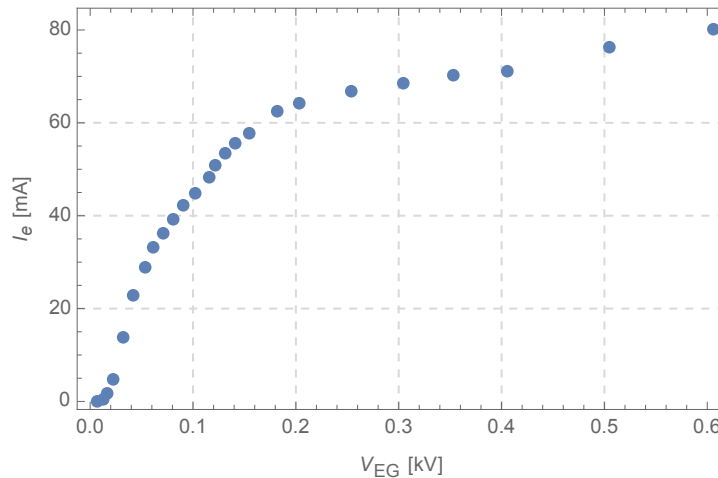

Figure 16: Hydrogen electron current at 1 kW RF power, 1.4 Pa.

As shown in figure 17, the hydrogen perveance factor found by interpolation has a magnitude of 9.852×10^{-8} A $V^{-3/2}$.
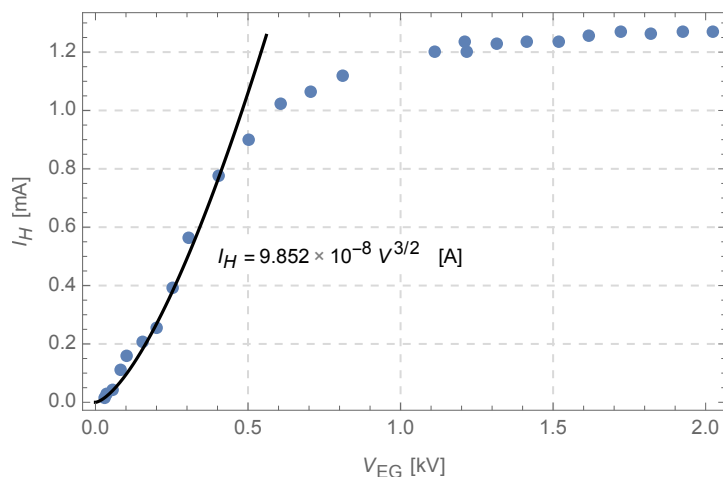
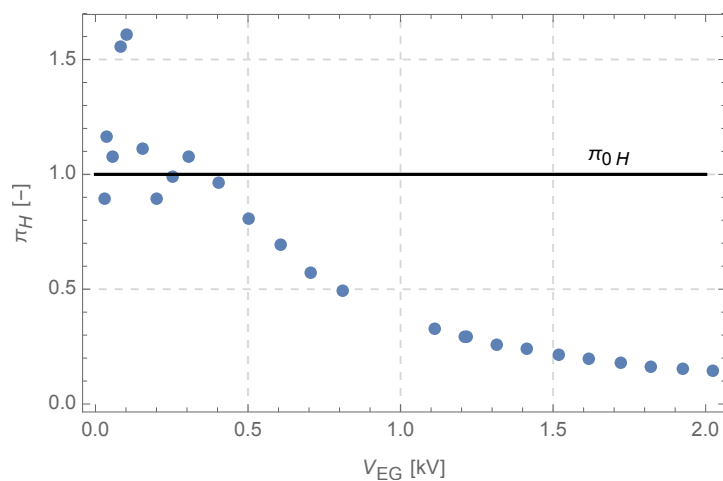Figure 17: Hydrogen negative ion current at 1 kW RF power, 1.4 Pa.

Figure 18: Hydrogen normalized perveance at 1 kW RF power, 1.4 Pa.

Oxygen operations

The data acquisitions with the heavier ion, were conducted at lower source pressure because oxygen requires less energy than hydrogen to inductively couple with the source, probably because of its higher electronegativity.

It was found that the extracted O^- current follows the CL law up to 1.2 kV at 1 kW RF power. Then, as for hydrogen, saturation occurs. Unfortunately, the electron current experienced saturation before the first acquisition point which is at 508 V, so it becomes impossible to estimate the fraction γ_{iO} in the CL region.

As shown in figure 19, the oxygen perveance factor found by interpolation has a magnitude of 3.2×10^{-8} A $V^{-3/2}$.
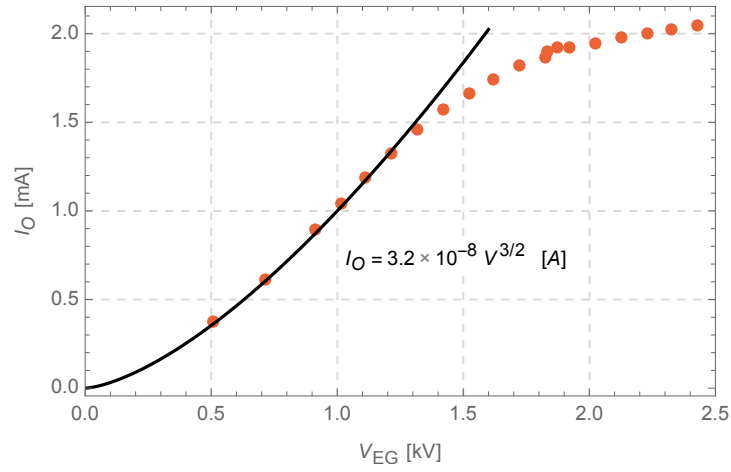
Figure 19: Oxigen negative ion current at 1 kW RF power, 0.35 Pa.

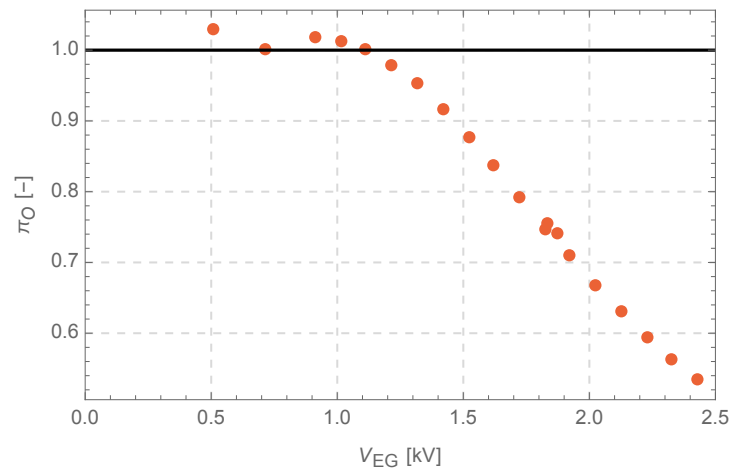

Figure 20: Oxigen normalized perveance at 1 kW RF power, 0.35 Pa.

3.3 Source analysis

The beam model shown in section 2 and the classical CL law both allow to calculate the space charge current limit assuming that unlimited amount of ions can be produced by the source. This assumption ceases to be valid if the extraction system outperforms the **source production capacity**.

The source of NIO1 has several parameters on which the operator can act in order to change plasma properties. However, RF power P_{RF} and source pressure p are the main ones: by increasing input power, more energy is transferred to the plasma particles, while by enhancing the pressure, higher collision frequency is obtained. Inside particular P_{RF} and p intervals, the extractable negative ion production is a monotonically growing function:

$$f[P_{\mathrm{RF}}, p]$$

For low extraction voltages, only particles in the meniscus zone are extracted and the current is determined by the Child-Langmuir Law. However, the extracted current cannot grow endlessly: at higher extractions voltages, once all these negative particles have been extracted, a flux from the inner source region to the PG is necessary induced in order to keep the neutrality in the meniscus zone. These particles are therefore extracted at a slower pace and the and the normalized perveance starts to decrease under the unity. Moreover, as the meniscus is pulled towards the source, the beam optics has to be corrected in order to avoid the under-perveant situation by increasing the source pressure, the RF power or both.

By combining data from oxygen scans at different RF power, it was possible to estimate how the saturation limit varies at constant pressure. The results are shown graphically in figure 21, the interpolations are the followings:

$$I_{500\mathrm{W}} = 0.9(1 - e^{-0.949 V_{\mathrm{EG}}})$$
$$I_{700\mathrm{W}} = 1.568(1 - e^{-0.997 V_{\mathrm{EG}}})$$
$$I_{900\mathrm{W}} = 2.311(1 - e^{-0.705 V_{\mathrm{EG}}})$$
$$I_{1000\mathrm{W}} = 2.569(1 - e^{-0.692 V_{\mathrm{EG}}})$$

A completely different dataset is also shown in fig. 22 to prove that this saturation is a general phenomenon. In fact, the Penning source, located at the Rutherford Appleton Laboratory in UK [13], uses a gas discharge as the negative ion source. Several V_{EG} scans at different discharge currents was performed in order to find how the saturation limit changes. It was found that the saturation current is almost proportional to the arc current, with the exception of the curve at 40 A which is altered because of an anomalous beam divergence. Whatever is the relation between the source parameter and the extracted current, this findings unequivocally confirms the concept of the source production bottleneck, in analogy with the thermionic emission.

In figure 6, the typical behavior of the current extracted from a hot cathode that is emitting by thermionic emission was showed. As the extraction voltage is increased, the transition between CL law (the space charge limit) and the Richardson's law (source production limit) happens in a similar fashion.
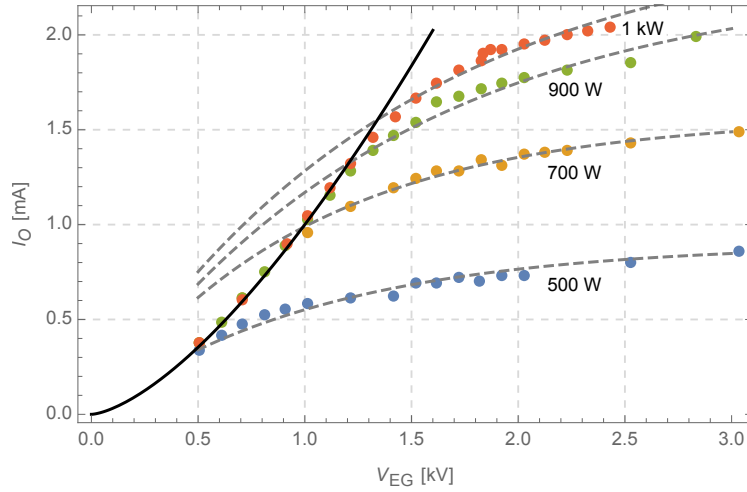
Figure 21: Oxigen negative ion current at different RF power, 0.35 Pa.
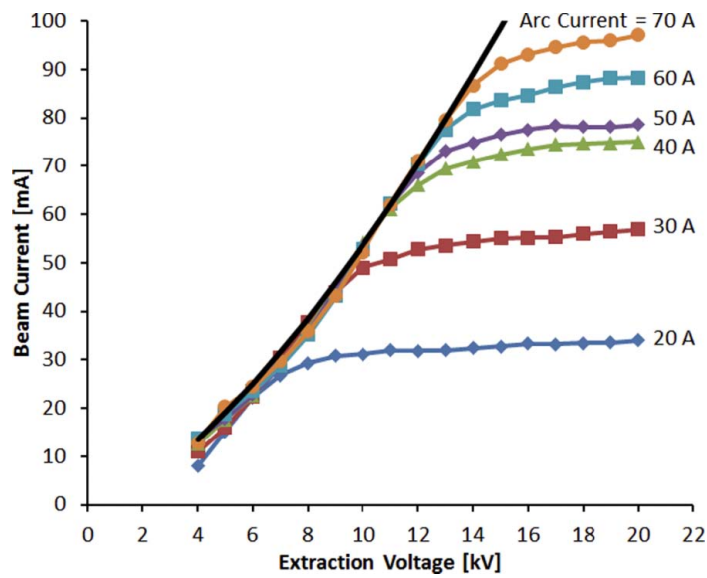

Figure 22: Perveance scans of the Rutherford Appleton Laboratory Penning ion source [13].

4 Conclusions

In the research field of the nuclear fusion, the ITER experiment is one of the most promising projects which can demonstrate the feasibility of a nuclear fusion power plant. The development of external heating systems is a fundamental step and requires an international cooperation. The ITER neutral beam injector prototype, that will operate at Consorzio RFX required preliminary studies, in order to validate numerical codes and test diagnostic systems. For this purpose, NIO1 a smaller and more flexible negative ion source was developed.

Due to the relative low input power and the absence of caesium oven, the accelerator is not used at its maximum capability. The extracted electron current is still too high compared to that of the ions and the beam has an intensity too low for being properly diagnosed. For this reasons the beam analysis could rely only on electrical measurements. The accelerator was tested using oxygen and hydrogen gasses.

Due to the restricted availability of data, this thesis developed as a theoretical work capable of describing the beam acceleration under a very large number of operation conditions. The fact that it is analytical and adimensional allows to use it for the precise computation of the maximum obtainable performances of most the planar interface accelerators for any given particle, at any energy level and scale.

The theoretical basis of this work come from the study of thermionics, with a special focus to the Richardson's and Child's laws. In particular, the Child-Langmuir current limit is generalized under a novel approach thanks to the parametrization of the model under both the spacial and the temporal dimensions. The model is then presented in its graphical form because of the large number of features it can describe.

In the empirical section of this work, the NIO1 experiment was used as a test bench for the model. The findings suggest that the experimental apparatus operates with a insufficient ion production capacity. This problem will by partly addressed by installing the caesium oven. Since the model can agree with the experimental results only for low extraction voltages, in the last section an explanation of the saturation phenomenon is proposed by a thermionic emission analogy.

A Mathematica codes

SPM code

```
J[s_] := J0
ψ[s_] := ψ0 + J0 s
v[s_] := v0 + ψ0 s + J0 s ^ 2 / 2
x[s_] := v0 s + ψ0 s ^ 2 / 2 + J0 s ^ 3 / 6
V[s_] := - (v[s] ^ 2 - v0 ^ 2) / 2
ρ[s_] := J[s] / v[s]
q = -1.60217653 10^-19; (*elementary electric charge (with sign!) [C]*)
ε0 = 8.85418782 × 10^-12; (*vacuum permittivity [F/m]*)
u = 1.66054 × 10^-27; (*atomic mass base unit*)
mH = 1.00794 u; (*monoatomic Hydrogen mass*)
mO = 15.9994 u; (*monoatomic Oxygen mass*)
me = 9.1093826 × 10^-31; (*Electron mass*)
m = mH; (*actual particle mass*)
vscale = L / T; (*velocity scale factor [m/s]*)
Vscale = m L ^ 2 / (q T ^ 2); (*electric potential scale factor [m/s]*)
ψscale = m L / (q T ^ 2); (*E-field scale factor [kg m/C s^2]*)
ρscale = m ε0 / (q T ^ 2); (*charge density scale factor [kg/V m s^2]*)
Jscale = m ε0 L / (q T ^ 3); (*current density scale factor [kg/V m s^3]*)
```

Figure 23: Model definition.

```
(*sost is the set of substitutions that needs to be applied to the adimentional
 equations in order to give SI results*)

sost = {d → 1, v0 → 0, V1 → 0.1 i ^ 2, sd → CubeRoot[6 d / J0], ψ0 → - (2 v0)/sd, J0 → 2/(9 d^2) (v0 + Sqrt[v0^2 + 2 V1])^3};

SetOptions[ParametricPlot, {Axes → False, Frame → True, AspectRatio → 0.618, GridLines → Automatic,
   GridLinesStyle → Directive[LightGray, Dashed]}, ImageSize → 350];
{Show@Table[ParametricPlot[{x[s], V[s]} //. sost, {s, 0, sd //. sost}, PlotRange → {{0, 1}, All},
    FrameLabel → {"x/d", "V/Vscale"}, PlotStyle → ColorData[10, i]], {i, 1, 8}],
 Show@Table[ParametricPlot[{x[s], ψ[s]} //. sost, {s, 0, sd //. sost}, PlotRange → {{0, 1}, All},
    FrameLabel → {"x/d", "E/Escale"}, PlotStyle → ColorData[10, i]], {i, 1, 8}],
 Show@Table[ParametricPlot[{x[s], v[s]} //. sost, {s, 0, sd //. sost}, PlotRange → {{0, 1}, All},
    FrameLabel → {"x/d", "v/vscale"}, PlotStyle → ColorData[10, i]], {i, 1, 8}],
 Show@Table[ParametricPlot[{x[s], ρ[s]} //. sost, {s, 0, sd //. sost}, PlotRange → {{0, 1}, {0, 10}},
    FrameLabel → {"x/d", "ρ/ρscale"}, PlotStyle → ColorData[10, i]], {i, 1, 8}],
 Show@Table[ParametricPlot[{x[s], s / sd} //. sost, {s, 0, sd //. sost}, PlotRange → {{0, 1}, {0, 1}},
    FrameLabel → {"x/d", "s/s_d"}, PlotStyle → ColorData[10, i]], {i, 1, 8}],
 Show@Table[ParametricPlot[{x[s], J0} //. sost, {s, 0, sd //. sost}, PlotRange → {{0, 1}, All},
    FrameLabel → {"x/d", "J/Jscale"}, PlotStyle → ColorData[10, i]], {i, 1, 8}]}
```

Figure 24: Case 1: adimensional for $v_0 = 0$

```
(*sost is the set of substitutions that needs to be applied to the adimentional
 equations in order to give SI results*)

sost = {d → 1, v0 → 2 × 10^5, V1 → 0.1 i ^ 2, sd → CubeRoot[6 d / J0], ψ0 → - (2 v0)/sd,

   J0 → 2/(9 d^2) (v0 + Sqrt[v0^2 + 2 V1])^3};

SetOptions[ParametricPlot, {Axes → False, Frame → True, AspectRatio → 0.618, GridLines → Automatic,
   GridLinesStyle → Directive[LightGray, Dashed]}, ImageSize → 350];
{Show@Table[ParametricPlot[{x[s], V[s]} //. sost, {s, 0, sd //. sost}, PlotRange → {{0, 1}, All},
    FrameLabel → {"x/d", "V/Vscale"}, PlotStyle → ColorData[10, i]], {i, 1, 8}],
 Show@Table[ParametricPlot[{x[s], ψ[s]} //. sost, {s, 0, sd //. sost}, PlotRange → {{0, 1}, All},
    FrameLabel → {"x/d", "E/Escale"}, PlotStyle → ColorData[10, i]], {i, 1, 8}],
 Show@Table[ParametricPlot[{x[s], v[s]} //. sost, {s, 0, sd //. sost}, PlotRange → {{0, 1}, All},
    FrameLabel → {"x/d", "v/vscale"}, PlotStyle → ColorData[10, i]], {i, 1, 8}],
 Show@Table[ParametricPlot[{x[s], ρ[s]} //. sost, {s, 0, sd //. sost}, PlotRange → {{0, 1}, {0, 10}},
    FrameLabel → {"x/d", "ρ/ρscale"}, PlotStyle → ColorData[10, i]], {i, 1, 8}],
 Show@Table[ParametricPlot[{x[s], s / sd} //. sost, {s, 0, sd //. sost}, PlotRange → {{0, 1}, {0, 1}},
    FrameLabel → {"x/d", "s/s_d"}, PlotStyle → ColorData[10, i]], {i, 1, 8}],
 Show@Table[ParametricPlot[{x[s], J0} //. sost, {s, 0, sd //. sost}, PlotRange → {{0, 1}, All},
    FrameLabel → {"x/d", "J/Jscale"}, PlotStyle → ColorData[10, i]], {i, 1, 8}]}
```

Figure 25: Case 2: adimensional for $v_0 \neq 0$

```
(*sost is the set of substitutions that needs to be applied to the adimentional
 equations in order to give SI results*)
sost = {T → 1, L → 1, d → 0.005 / L, v0 → 2 × 10^5 / vscale, V1 → 250 i / Vscale, sd → CubeRoot[6 d / J0],

       ψ0 → - (2 v0)/sd, J0 → 2/(9 d^2) (v0 + Sqrt[v0^2 - 2 V1])^3};
SetOptions[ParametricPlot, {Axes → False, Frame → True, AspectRatio → 0.618, GridLines → Automatic,
    GridLinesStyle → Directive[LightGray, Dashed]}, ImageSize → 350];

{Show@Table[ParametricPlot[{x[s] * 10^3 L, (V[s] - V[sd]) * 10^-3 Vscale} //. sost,
    {s, 0, sd //. sost}, PlotRange → All, PlotStyle → ColorData[10, i],
    FrameLabel → {"x [mm]", "V [kV]"}], {i, 1, 8}],
 Show@Table[ParametricPlot[{x[s] * 10^3 L, ψ[s] * 10^-3 ψscale} //. sost, {s, 0, sd //. sost},
    PlotRange → All, PlotStyle → ColorData[10, i], FrameLabel → {"x [mm]", "E [kV/m]"}], {i, 1, 8}],
 Show@Table[ParametricPlot[{x[s] * 10^3 L, v[s] * 10^-3 vscale} //. sost, {s, 0, sd //. sost},
    PlotRange → All, PlotStyle → ColorData[10, i], FrameLabel → {"x [mm]", "v [km/s]"}], {i, 1, 8}],
 Show@Table[ParametricPlot[{x[s] * 10^3 L, ρ[s] * 10^3 ρscale} //. sost, {s, 0, sd //. sost},
    PlotRange → All, PlotStyle → ColorData[10, i], FrameLabel → {"x [mm]", "ρ×10^3 [C/m^3]"}],
   {i, 1, 8}],
 Show@Table[ParametricPlot[{x[s] * 10^3 L, s / sd * T} //. sost, {s, 0, sd //. sost},
    PlotRange → All, PlotStyle → ColorData[10, i], FrameLabel → {"x [mm]", "s/s_d [-]"}], {i, 1, 8}],
 Show@Table[ParametricPlot[{x[s] * 10^3 L, J[s] * Jscale} //. sost, {s, 0, sd //. sost},
    PlotRange → All, PlotStyle → ColorData[10, i], FrameLabel → {"x [mm]", "J [A/m^2]"}], {i, 1, 8}]}
```

Figure 26: Case 3: physical dimensions for $v_0 \neq 0$

TPM code

```
ψ[s_] := ψ0 + J0 s

xi[s_] := vi0 s + γi ( ψ0/2 s^2 + J0/6 s^3 )

vi[x_] := vi0 + γi ( ψ0 s + J0/2 s^2 ) /. s → InverseFunction[xi][x]

V[x_] := - 1/(2 γi) (vi[x]^2 - vi0^2)

ρ[x_] := J0 γe/vi[x] ( 1/( Sqrt[ (γe mi)/(γi me) ] Sqrt[ 1 - 1/vi[x]^2 ( vi0^2 - ve0^2 (γi me)/(γe mi) ) ] ) + γi/γe )

ve[x_] := vi[x] Sqrt[ (γe mi)/(γi me) ] Sqrt[ 1 - 1/vi[x]^2 ( vi0^2 - ve0^2 (γi me)/(γe mi) ) ]


q = -1.60217653 10^-19;  (*elementary electric charge (with sign!) [C]*)
ε0 = 8.85418782 × 10^-12;  (*vacuum permittivity [F/m]*)
u = 1.66054 × 10^-27;  (*atomic mass base unit*)
mH = 1.00794 u;  (*monoatomic Hydrogen mass*)
mO = 15.9994 u;  (*monoatomic Oxygen mass*)
me = 9.1093826 × 10^-31;  (*Electron mass*)
m = mH;  (*actual particle mass*)
vscale = L/T;  (*velocity scale factor [m/s]*)
Vscale = m L^2 / (q T^2);  (*electric potential scale factor [m/s]*)
ψscale = m L / (q T^2);  (*E-field scale factor [kg m/C s^2]*)
ρscale = m ε0 / (q T^2);  (*charge density scale factor [kg/V m s^2]*)
Jscale = m ε0 L / (q T^3);  (*current density scale factor [kg/V m s^3]*)
```

Figure 27: Model definition.

```mathematica
sost = {T → 1, L → 1, d → 0.005 / L, vi0 → 0 / vscale, ve0 → vi0 √(γe mi)/(γi me) , V1 → 2000 / Vscale,

    sd → CubeRoot[6 d / (J0 γi)], ψ0 → - (2 vi0)/(γi sd) , J0 → 2/(γi 9 d²) (vi0 + Sqrt[vi0² - 2 γi V1])³, γi → i / 10,

    γe → 1 - γi,
    γ → γi / γe};
SetOptions[ParametricPlot, {Axes → False, Frame → True, AspectRatio → 0.618,
    GridLines → Automatic, GridLinesStyle → Directive[LightGray, Dashed]}, ImageSize → 350];
SetOptions[Plot, {Axes → False, Frame → True, AspectRatio → 0.618, GridLines → Automatic,
    GridLinesStyle → Directive[LightGray, Dashed]}, ImageSize → 350];
SetOptions[LogPlot, {Axes → False, Frame → True, AspectRatio → 0.618, GridLines → Automatic,
    GridLinesStyle → Directive[LightGray, Dashed]}, ImageSize → 350];

{Show@Table[ParametricPlot[{x * 10³ L, (V[x] - V[d]) * 10⁻³ Vscale} //. sost, {x, 0, d //. sost},
    PlotRange → All, PlotStyle → ColorData[10, i], FrameLabel → {"x [mm]", "V [kV]"}], {i, 1, 9, 2}],
 Show@Table[ParametricPlot[{xi[s] * 10³ L, -ψ[s] * 10⁻³ ψscale} //. sost, {s, 0, sd //. sost},
    PlotRange → All, PlotStyle → ColorData[10, i], FrameLabel → {"x [mm]", "E [kV/m]"}], {i, 1, 9, 2}],
 Show@Table[ParametricPlot[{x * 10³ L, vi[x] * 10⁻³ vscale} //. sost, {x, 0, d //. sost},
    PlotRange → All, PlotStyle → ColorData[10, i], FrameLabel → {"x [mm]", "vᵢ [km/s]"}], {i, 1, 9}],
 Show@Table[ParametricPlot[{x * 10³ L, ve[x] * 10⁻³ vscale} //. sost, {x, 0, d //. sost},
    PlotRange → All, PlotStyle → ColorData[10, i], FrameLabel → {"x [mm]", "vₑ [km/s]"}], {i, 1, 9}],
 Show@Table[LogPlot[ (-γi J0)/(vi[x * 10⁻³]) * ρscale //. sost, {x, 0, d * 10³ //. sost}, PlotRange → {10⁻⁵, 10⁻¹},

    PlotStyle → ColorData[10, i], FrameLabel → {"x [mm]", "ρᵢ [C/m³]"}], {i, 1, 9}],
 Show@Table[LogPlot[ (-γe J0)/(ve[x * 10⁻³]) * ρscale //. sost, {x, 0, d * 10³ //. sost}, PlotRange → {10⁻⁶, 10⁻⁴},

    PlotStyle → ColorData[10, i], FrameLabel → {"x [mm]", "ρₑ [C/m³]"}], {i, 1, 9}],
 Show@Table[ParametricPlot[{xi[s] * 10³ L, s / sd * T} //. sost, {s, 0, sd //. sost},
    PlotRange → All, PlotStyle → ColorData[10, i], FrameLabel → {"x [mm]", "s/s_d [-]"}], {i, 1, 9, 2}],
 Show@Table[Plot[J0 * Jscale //. sost, {x, 0, d * 10³ //. sost}, PlotRange → All,
    PlotStyle → ColorData[10, i], FrameLabel → {"x [mm]", "J [A/m²]"}], {i, 1, 9}]}
```

Figure 28: Case 1: physical dimensions for $v_0 = 0$

```mathematica
sost = {T → 1, L → 1, d → 0.005 / L, vi0 → 2 × 10^4 / vscale, ve0 → vi0 Sqrt[γe mi / (γi me)], V1 → 2000 / Vscale,
   sd → CubeRoot[6 d / (J0 γi)], ψ0 → - 2 vi0 / (γi sd), J0 → 2 / (γi 9 d^2) (vi0 + Sqrt[vi0^2 - 2 γi V1])^3, γi → i / 10,
   γe → 1 - γi,
   γ → γi / γe};
SetOptions[ParametricPlot, {Axes → False, Frame → True, AspectRatio → 0.618,
   GridLines → Automatic, GridLinesStyle → Directive[LightGray, Dashed]}, ImageSize → 350];
SetOptions[Plot, {Axes → False, Frame → True, AspectRatio → 0.618, GridLines → Automatic,
   GridLinesStyle → Directive[LightGray, Dashed]}, ImageSize → 350];
SetOptions[LogPlot, {Axes → False, Frame → True, AspectRatio → 0.618, GridLines → Automatic,
   GridLinesStyle → Directive[LightGray, Dashed]}, ImageSize → 350];

{Show@Table[ParametricPlot[{x * 10^3 L, (V[x] - V[d]) * 10^-3 Vscale} //. sost, {x, 0, d //. sost},
    PlotRange → All, PlotStyle → ColorData[10, i], FrameLabel → {"x[mm]", "V [kV]"}], {i, 1, 9, 2}],
 Show@Table[ParametricPlot[{xi[s] * 10^3 L, -ψ[s] * 10^-3 ψscale} //. sost, {s, 0, sd //. sost},
    PlotRange → All, PlotStyle → ColorData[10, i], FrameLabel → {"x [mm]", "E [kV/m]"}], {i, 1, 9, 2}],
 Show@Table[ParametricPlot[{x * 10^3 L, vi[x] * 10^-3 vscale} //. sost, {x, 0, d //. sost},
    PlotRange → All, PlotStyle → ColorData[10, i], FrameLabel → {"x [mm]", "v_i [km/s]"}], {i, 1, 9}],
 Show@Table[ParametricPlot[{x * 10^3 L, ve[x] * 10^-3 vscale} //. sost, {x, 0, d //. sost},
    PlotRange → All, PlotStyle → ColorData[10, i], FrameLabel → {"x [mm]", "v_e [km/s]"}], {i, 1, 9}],
 Show@Table[LogPlot[-γi J0 / vi[x * 10^-3] * ρscale //. sost, {x, 0, d * 10^3 //. sost}, PlotRange → {10^-5, 10^-1},
    PlotStyle → ColorData[10, i], FrameLabel → {"x [mm]", "ρ_i [C/m^3]"}], {i, 1, 9}],
 Show@Table[LogPlot[-γe J0 / ve[x * 10^-3] * ρscale //. sost, {x, 0, d * 10^3 //. sost}, PlotRange → {10^-6, 10^-4},
    PlotStyle → ColorData[10, i], FrameLabel → {"x [mm]", "ρ_e [C/m^3]"}], {i, 1, 9}],
 Show@Table[ParametricPlot[{xi[s] * 10^3 L, s / sd * T} //. sost, {s, 0, sd //. sost},
    PlotRange → All, PlotStyle → ColorData[10, i], FrameLabel → {"x [mm]", "s/s_d [-]"}], {i, 1, 9, 2}],
 Show@Table[Plot[J0 * Jscale //. sost, {x, 0, d * 10^3 //. sost}, PlotRange → All,
    PlotStyle → ColorData[10, i], FrameLabel → {"x [mm]", "J [A/m^2]"}], {i, 1, 9}]}
```

Figure 29: Case 2: physical dimensions for $v_0 \neq 0$

```mathematica
sost = {T → 1, L → 1, d → 0.005 / L, V1 → 2000 Exp[-i] / Vscale, ve0 → vi0 Sqrt[γe mi / (γi me)],
   sd → CubeRoot[6 d / (J0 γi)], ψ0 → - 2 vi0 / (γi sd), J0 → 2 / (γi 9 d^2) (vi0 + Sqrt[vi0^2 - 2 γi V1])^3, γi → 0.25,
   γe → 1 - γi,
   γ → γi / γe};
ListLogLogPlot[
 {Table[{V1 * Vscale, -J0 γi * Jscale * 9 π * 0.003^2 * 1000} //. sost, {i, 0, 5, 0.5}] /. vi0 → 0,
  Table[{V1 * Vscale, -J0 γi * Jscale * 9 π * 0.003^2 * 1000} //. sost, {i, 0, 5, 0.5}] /. vi0 → 10^4 / vscale //.
   sost, Table[{V1 * Vscale, -J0 γi * Jscale * 9 π * 0.003^2 * 1000} //. sost, {i, 0, 5, 0.5}] /.
   vi0 → 3 × 10^4 / vscale //. sost,
  Table[{V1 * Vscale, -J0 γi * Jscale * 9 π * 0.003^2 * 1000} //. sost, {i, 0, 5, 0.5}] /.
   vi0 → 5 × 10^4 / vscale //. sost}, Joined → True, Frame → True, AspectRatio → 0.618,
 GridLines → Automatic, GridLinesStyle → Directive[Gray, Dashed],
 FrameLabel → {"ΔV [kV]", "I_{H,MAX} [mA]"}, ImageSize → 400]
```

Figure 30: Plot of the maximum current with the initial velocity parameter.

References

[1] G. Czisch, "Affordable renewable electricity supply for europe and its neighbors," *Claverton Energy Conference*, 2008. (Cited at page 1)

[2] "World energy outlook 2016." International Energy Agency. (Cited at page 1)

[3] "Rapporto statistico "energia da fonti rinnovabili in italia - 2014"." Gestore Servizi Energetici. (Cited at page 1)

[4] M. Kikuchi, K. Lackner, and M. Q. Tran, *Fusion Physics*. International Atomic Energy Agency, 2012. (Cited at page 2)

[5] V. Toigo, R. Piovan, S. D. Bello, and S. Sandri, "A substantial step forward in the realization of the iter hnb system: The iter nbi test facility," *DOI: 10.1016/j.fusengdes.2016.11.007*, 2016. (Cited at page 3)

[6] D. Mazon, C. Fenzi, and R. Salbot, "As hot as it gets," *Nature Physics*, vol. 12, pp. 14–17, 2016. (Cited at page 3)

[7] A. Delorenzi, D. Marcuzzi, R. Piovan, P. Sonato, V. Toigo, and P. Zaccaria, "Status of the iter heating neutral beam system," *Nuclear Fusion*, vol. 49, p. 045006, 2009. (Cited at page 4)

[8] M. Bacal and M. Wada, "Negative hydrogen ion production mechanisms," *Applied physics reviews 2.2*, p. 021305, 2015. (Cited at page 4)

[9] P.Veltri, E. Sartori, M. Barbisan, M. Cavenago, G. Serianni, and B. Zaniol, "Study of electron transport across the magnetic filter of nio1 negative ion source," *submitted to AIP conference proceedings of the 5th International Symposium on Negative Ions, Beams and Sources (NIBS2016)*, 2016. (Cited at page 4)

[10] T. Kirkman, *Thermionic emission*. Saint John's University, 2009. online at: http://www.physics.csbsju.edu/tk/370/manual14.pdf. (Cited at page 7)

[11] G. Jaffé, "On the currents carried by electrons of uniform initial velocity," *Physical review*, vol. 65, p. 91, 1844. (Cited at page 15)

[12] R. R. Puri, D. Biswas, and R. Kumar, "Generalisation of the child-langmuir law for nonzero injection velocities in a planar diode," *Physics of plasma*, march 2004. (Cited at pages 15 and 16)

[13] S. R. Lawrie, D. C. Faircloth, P. Letchford, O. Whitehead, and T. Wood, "Detailed beam and plasma measurements on the vessel for extraction and source plasma analyses (vespa) penning h - ion source," *Review of scientific instruments*, vol. 87, p. 02B122, 2016. (Cited at pages 31 and 32)